

1 Neuronal DAMPs exacerbate neurodegeneration via astrocytic RIPK3 signaling

2

3 Nydia P. Chang<sup>1</sup>, Evan M. DaPrano<sup>1</sup>, Wesley R. Evans<sup>1,2</sup>, Marialaina Nissenbaum<sup>3</sup>, Micheal  
4 McCourt<sup>1</sup>, Diego Alzate<sup>1</sup>, Marissa Lindman<sup>1</sup>, Tsui-Wen Chou<sup>1</sup>, Colm Atkins<sup>1</sup>, Alexander W.  
5 Kusnecov<sup>3</sup>, Rafiq Huda<sup>1,2</sup>, and Brian P. Daniels<sup>1\*</sup>

6

7 <sup>1</sup> Department of Cell Biology and Neuroscience, Rutgers University, Piscataway, NJ 08854,  
8 USA

9 <sup>2</sup> W. M. Keck Center for Collaborative Neuroscience, Rutgers University, Piscataway, NJ  
10 08854, USA

11 <sup>3</sup> Department of Psychology, Rutgers University, Piscataway, NJ 08854, USA

12

13

14 \*Correspondence:  
15 Brian Daniels  
16 [b.daniels@rutgers.edu](mailto:b.daniels@rutgers.edu)

17

18

19

20 **Abstract**

21           Astrocyte activation is a common feature of neurodegenerative diseases. However, the  
22 ways in which dying neurons influence the activity of astrocytes is poorly understood. RIPK3  
23 signaling has recently been described as a key regulator of neuroinflammation, but whether  
24 this kinase mediates astrocytic responsiveness to neuronal death has not yet been studied.  
25 Here, we used the MPTP model of Parkinson's disease to show that activation of astrocytic  
26 RIPK3 drives dopaminergic cell death and axon damage. Transcriptomic profiling revealed that  
27 astrocytic RIPK3 promoted gene expression associated with neuroinflammation and  
28 movement disorders, and this coincided with significant engagement of DAMP signaling. Using  
29 human cell culture systems, we show that factors released from dying neurons signal through  
30 RAGE to induce RIPK3-dependent astrocyte activation. These findings highlight a mechanism  
31 of neuron-glia crosstalk in which neuronal death perpetuates further neurodegeneration by  
32 engaging inflammatory astrocyte activation via RIPK3.

33

## 34 Introduction

35 Recent work has identified a central role for neuroinflammation in the pathogenesis of  
36 neurological disease, including major neurodegenerative disorders such as Alzheimer's and  
37 Parkinson's disease<sup>1,2</sup>. Although glial cells are critical regulators of neuroinflammation,  
38 activated glia serve complex roles during disease, including both protective and pathogenic  
39 functions<sup>3</sup>. Among glial cells, astrocytes are the most abundant cell type in the central nervous  
40 system (CNS), where they support homeostasis via wide-ranging effects on  
41 neurotransmission, neurovascular function, and metabolism<sup>4</sup>. However, following an  
42 inflammatory insult, astrocytes can enter "reactive" states associated with disease  
43 pathogenesis<sup>5</sup>. While astrocyte activation is likely highly plastic and context-dependent, it is  
44 now widely accepted that astrocytes can take on inflammatory transcriptional states during  
45 disease that are associated with the conferral of neurotoxic activity and suppression of normal  
46 homeostatic functions<sup>6</sup>. Despite this understanding, the molecular mechanisms that govern  
47 astrocyte reactivity during neurodegenerative disease, and particularly those factors that most  
48 directly exacerbate disease progression, remain poorly understood<sup>7</sup>.

49 We and others have recently identified receptor-interacting serine/threonine protein  
50 kinase-3 (RIPK3) as a key regulator of inflammation in the CNS<sup>8-10</sup>. RIPK3 signaling is  
51 canonically associated with necroptotic cell death, which is induced via the activation of mixed  
52 lineage kinase domain-like protein (MLKL)<sup>11</sup>. While RIPK3-dependent necroptosis has been  
53 implicated in the pathogenesis of several neurological disorders, RIPK3 also appears to  
54 promote neuroinflammatory processes via necroptosis-independent mechanisms, including the  
55 coordination of inflammatory transcription in multiple CNS cell types<sup>12-18</sup>. While necroptosis-  
56 independent roles for RIPK3 signaling in astrocytes have not been thoroughly studied, we  
57 have previously shown that pathogenic  $\alpha$ -synuclein fibrils activate RIPK3 signaling in human  
58 midbrain astrocyte cultures, resulting in NF- $\kappa$ B-mediated transcriptional activation without  
59 inducing astrocytic necroptosis<sup>14</sup>. However, whether RIPK3 controls astrocyte transcriptional  
60 activation and function in models of neurodegenerative disease *in vivo* is unknown.

61 The importance of neuron-glia communication during CNS disease states has also  
62 gained significant recognition in recent work<sup>19-22</sup>. A particularly important goal in this area is  
63 defining the stimuli that induce inflammatory signaling in the "sterile" setting of  
64 neurodegeneration. One potential stimulus underlying inflammatory astrocyte activation during  
65 neurodegeneration are factors derived from dead and dying neurons, themselves. These  
66 factors include damage-associated molecular patterns (DAMPs), molecules released from  
67 damaged cells that serve as endogenous danger signals that elicit potent innate immune  
68 activation in neighboring cells<sup>23,24</sup>. DAMP release has been associated with numerous  
69 inflammatory diseases, including neurodegenerative disorders<sup>25-28</sup>. However, whether and how  
70 neuron-derived DAMPs impact astrocyte function during neurodegenerative disease has not  
71 been thoroughly studied to date.

72 Here, we define a new role for RIPK3 signaling in mediating astrocyte activation  
73 downstream of neuronal DAMP release. We utilize the 1-methyl-4-phenyl-1,2,3,6-  
74 tetrahydropyridine (MPTP) model of Parkinson's disease, in which cell death can be selectively

75 induced in dopaminergic neurons *in vivo*, to show that induction of neuronal cell death results  
76 in RIPK3-dependent astrocyte activation, which in turn exacerbates ongoing  
77 neurodegeneration. Transcriptional profiling revealed a robust RIPK3-dependent inflammatory  
78 signature in astrocytes exposed to dying neuron-derived factors, and this occurred  
79 independently of astrocytic MLKL. Mechanistically, we show that factors released from dying  
80 dopaminergic neurons activate receptor for advanced glycation endproducts (RAGE) on  
81 midbrain astrocytes. RAGE signaling, in turn, was required for RIPK3 activation, inflammatory  
82 transcription, and the conferral of neurotoxic activity in midbrain astrocytes following exposure  
83 to neuronal DAMPs. Our findings suggest a feed-forward mechanism that perpetuates  
84 neurodegeneration via the DAMP-dependent activation of RIPK3-dependent inflammation and  
85 neurotoxicity in astrocytes. These results highlight an important mechanism of neuron-glia  
86 crosstalk, with implications for the prevention and treatment of neurodegenerative disease.

87

## 88 **Results**

89

### 90 *Astrocytic RIPK3 signaling promotes pathogenesis in the MPTP model of Parkinson's disease*

91 To examine the impact of astrocytic RIPK3 signaling in response to neuronal cell death,  
92 we subjected mice with astrocyte-specific deletion of *Ripk3* (*Ripk3<sup>fl/fl</sup> Aldh111<sup>Cre+</sup>*) and littermate  
93 controls to treatment with MPTP, a neurotoxin that selectively induces death in dopaminergic  
94 neurons<sup>29,30</sup>. MPTP administration resulted in significant loss of tyrosine hydroxylase (TH)  
95 immunoreactivity in the substantia nigra pars compacta (SNpc) of control animals, consistent  
96 with the depletion of dopaminergic neurons in this region (Figure 1A-B). Strikingly, however,  
97 *Ripk3<sup>fl/fl</sup> Aldh111<sup>Cre+</sup>* mice exhibited greatly reduced dopaminergic neuron loss following MPTP  
98 treatment, suggesting a role for astrocytic RIPK3 in exacerbating neuronal death in this model.  
99 We also observed a significant loss of TH<sup>+</sup> dopaminergic axons in the striatum of control  
100 animals (Figure 1C-D), along with increased frequencies of TH<sup>+</sup> axons immunoreactive for  
101 SMI32, a marker of axonal degeneration<sup>31-33</sup> (Figure 1E). This phenotype was also greatly  
102 ameliorated in *Ripk3<sup>fl/fl</sup> Aldh111<sup>Cre+</sup>* mice. To test whether these differences in dopaminergic  
103 neuron loss were associated with differences in motor function, we next subjected mice to the  
104 vertical grid maze, a motor task previously shown to be sensitive to perturbations of  
105 dopaminergic circuits<sup>34,35</sup>. Strikingly, MPTP-treated control mice exhibited significantly impaired  
106 performance in the vertical grid maze (Figure 1F-G), while mice lacking astrocytic *Ripk3* did  
107 not. Improvements in dopaminergic neuron loss and motor performance in *Ripk3<sup>fl/fl</sup> Aldh111<sup>Cre+</sup>*  
108 mice were not due to differential metabolism of MPTP compared to Cre- littermates, as we  
109 observed indistinguishable levels of the toxic metabolite of MPTP (MPP<sup>+</sup>) in midbrain  
110 homogenates derived from animals of both genotypes (Supplemental Figure 1). Together,  
111 these data suggest that astrocytic RIPK3 signaling exacerbates neuronal cell death following a  
112 neurotoxic insult.

113

114 *RIPK3 drives inflammatory transcriptional activation but not proliferation in midbrain astrocytes*

115 Given these findings, we next questioned how RIPK3 signaling influences the  
116 phenotype of astrocytes in the setting of MPTP administration. Immunohistochemical (IHC)  
117 staining of SNpc sections revealed increased GFAP staining in MPTP-treated control animals,  
118 consistent with astrocyte activation, and this effect was blocked in *Ripk3<sup>fl/fl</sup> Aldh111<sup>Cre+</sup>* mice  
119 (Figure 2A-B). To test whether enhanced GFAP staining indicated proliferative astrogliosis, we  
120 performed flow cytometric analysis of astrocytes in the midbrain of MPTP-treated animals,  
121 which revealed no differences in GLAST<sup>+</sup> astrocytes between genotypes (Figure 2C-D). These  
122 data suggested that enhanced GFAP staining was not due to increased numbers of astrocytes  
123 following MPTP administration, but rather a change in the astrocyte activation status. To test  
124 this idea, we performed qRT-PCR analysis of a panel of transcripts that we and others have  
125 shown to be associated with neurotoxic astrocyte activation in models of Parkinson's  
126 disease<sup>14,36,37</sup>. We observed upregulation of 10 out of 14 transcripts in our analysis panel in  
127 midbrain homogenates derived from MPTP-treated littermate controls, while this activation  
128 signature was essentially abolished in *Ripk3<sup>fl/fl</sup> Aldh111<sup>Cre+</sup>* mice (Figure 2E). In contrast, MPTP-  
129 treated *Mkl1<sup>-/-</sup>* mice showed equivalent levels of inflammatory transcript expression in the  
130 midbrain (Supplemental Figure 2). These data suggest that astrocytic RIPK3 signaling  
131 promotes an inflammatory transcriptional state in the midbrain following MPTP treatment,  
132 independently of MLKL and necroptosis.

133 We next more carefully assessed this idea by using a mouse line expressing RIPK3  
134 fused to two FKBP<sup>F36V</sup> domains that facilitate enforced oligomerization following treatment with  
135 a dimerization drug. This protein is expressed in a cell type-specific manner under the control  
136 of a lox-STOP-lox element in the *Rosa26* locus, while the endogenous *Ripk3* locus is left  
137 intact. Thus, this mouse line can be used as both a cell type-specific overexpression system  
138 while also facilitating forced chemogenetic activation of RIPK3 in cell types of interest *in*  
139 *vivo*<sup>12,13,38</sup>. We first questioned whether simple overexpression of RIPK3 in astrocytes would  
140 enhance the inflammatory transcriptional signature that occurs following MPTP administration.  
141 We observed that 4 neurotoxic astrocyte-associated transcripts exhibited augmented  
142 upregulation following MPTP administration in *Ripk3-2xFV<sup>fl/fl</sup> Aldh111<sup>Cre+</sup>* mice, including *Ccl5*,  
143 *Cd14*, *Cxcl10*, and *Psm8*, while 2 others exhibited trends towards increased expression that  
144 did not reach statistical significance (*Cd109*, *H2-D1*) (Figure 2F). To assess whether activation  
145 of astrocytic RIPK3 was sufficient to induce an inflammatory gene signature, we enforced  
146 RIPK3 activation in astrocytes via stereotactic delivery of B/B homodimerizer to the ventral  
147 midbrain of *Ripk3-2xFV<sup>fl/fl</sup> Aldh111<sup>Cre+</sup>* mice. B/B homodimerizer binds in a multivalent fashion  
148 to the FKBP<sup>F36V</sup> domains of RIPK3-2xFV proteins, driving their oligomerization, which is  
149 sufficient to induce RIPK3 kinase activity in the absence of any other stimulus<sup>39,40</sup> (Figure 2G-  
150 H). Enforced activation of RIPK3 in midbrain astrocytes *in vivo* resulted in induced expression  
151 of several neurotoxic astrocyte-associated transcripts, including *Cd14*, *Emp1*, *Gbp2*, *Lcn2*,  
152 *S100a10*, and *Srgn* (Figure 2I). Together, these data show that activation of RIPK3 in midbrain  
153 astrocytes drives their activation and the establishment of an inflammatory transcriptional  
154 signature.

155

156 *Astrocytic RIPK3 signaling has minimal impact on microgliosis in the MPTP model*

157 We next questioned whether the reduced expression of inflammatory genes observed in  
158 mice lacking astrocytic RIPK3 was associated with cell non-autonomous effects on other cell  
159 types in the setting of MPTP treatment. We thus performed IHC staining for IBA1, a marker of  
160 myeloid cells that largely labels microglia in the setting of sterile neurodegeneration<sup>41,42</sup>. This  
161 analysis revealed no differences in the overall coverage of IBA1 staining in the midbrain in  
162 *Ripk3<sup>fl/fl</sup> Aldh111<sup>Cre+</sup>* mice compared to littermate controls, though IBA1<sup>+</sup> cells did appear to  
163 exhibit a somewhat less ramified and more “activated” morphology following MPTP treatment  
164 in controls, but not conditional knockout, animals (Figure 3A-B). To assess changes to immune  
165 cells more carefully, we next performed flow cytometric analysis of leukocytes derived from the  
166 midbrain of MPTP-treated mice. This revealed essentially identical frequencies of CD45<sup>int</sup>  
167 CD11b<sup>+</sup> F4/80<sup>+</sup> microglia between genotypes (Figure 3C-D), confirming a lack of difference in  
168 microglial proliferation. Microglia exhibited no differences in common activation markers,  
169 including MHC-II (data not shown), between genotypes, although microglia derived from  
170 MPTP-treated *Ripk3<sup>fl/fl</sup> Aldh111<sup>Cre+</sup>* mice exhibited diminished expression of the costimulatory  
171 molecule CD80 compared to controls (Figure 3E-F), consistent with a less inflammatory  
172 phenotype. We observed very low frequencies of CD45<sup>hi</sup> infiltrating peripheral immune cells in  
173 the MPTP model (Figure 3C), the overall numbers of which did not differ by genotype (Figure  
174 3G). These data suggest that astrocytic RIPK3 signaling following MPTP administration likely  
175 induces neuroinflammation primarily through cell-intrinsic mechanisms, with modest cell non-  
176 autonomous effects on microglia.

177

178 *Astrocytic RIPK3 activation drives a transcriptomic state associated with inflammation and*  
179 *neurodegeneration in the midbrain*

180 To characterize how astrocytic RIPK3 shapes the neuroinflammatory state of the brain  
181 more thoroughly in the MPTP model, we also performed bulk RNA sequencing (RNA-seq) of  
182 isolated midbrain tissues derived from *Ripk3<sup>fl/fl</sup> Aldh111<sup>Cre+</sup>* and littermate controls. Principle  
183 component analysis revealed distinct separation of MPTP-treated control animals along PC1,  
184 while MPTP-treated conditional knockouts largely clustered with vehicle-treated animals of  
185 both genotypes (Figure 4A). Further analysis revealed a robust transcriptional response to  
186 MPTP in midbrain tissues of littermate control animals, including 452 significantly upregulated  
187 genes and 145 significantly downregulated genes (Figure 4B) compared to vehicle-treated  
188 controls. This transcriptional response was blunted in *Ripk3<sup>fl/fl</sup> Aldh111<sup>Cre+</sup>* mice, which exhibited  
189 only 195 significantly upregulated genes and 120 significantly downregulated genes compared  
190 to genotype-matched vehicle-treated animals (Figure 4C), suggesting that astrocytic RIPK3  
191 signaling drives a major portion of the tissue-wide transcriptional response to MPTP-induced  
192 neuronal cell death. In support of this idea, comparison of differentially expressed genes  
193 (DEGs) within MPTP-treated groups revealed 120 genes with significantly higher expression

194 and 252 genes with significantly lower expression in conditional knockouts compared to  
195 littermate controls (Figure 4D).

196 To better understand the functional relevance of these transcriptomic profiles, we  
197 performed Ingenuity Pathway Analysis (IPA) of genes differentially expressed between  
198 genotypes in MPTP-treated animals. This revealed significant enrichment of several disease  
199 and function terms with relevance to our study, including “Inflammation of the Central Nervous  
200 System,” “Progressive Neurological Disorder,” “Movement Disorders,” and others (Figure 4E).  
201 Comparisons of differentially regulated canonical pathways showed significant enrichment of  
202 pathways relating to programmed cell death and inflammation, as expected (Figure 4F).  
203 Notably, terms related to DAMP signaling were also highly enriched, including signaling by  
204 HMGB1 and S100 family proteins, both of which are factors released by dying and damaged  
205 cells that induce inflammation. Further analysis revealed significant upregulation of genes  
206 associated with astrocyte activation (Figure 4G), consistent with our previous qRT-PCR  
207 analysis. Comparisons of individual gene expression profiles for 2 selected IPA terms  
208 (Movement Disorders and DAMP signaling) revealed dozens of significant DEGs for both  
209 terms, characterized by a mix of both up- and down-regulated gene expression. Together, our  
210 RNA-seq analysis reveals a central role for astrocytic RIPK3 in promoting gene expression  
211 associated with neurodegeneration and neuroinflammation in the midbrain. Our findings also  
212 suggest a strong link between DAMP signaling and RIPK3-dependent neuroinflammation.

213

#### 214 *Secreted factors from dying neurons drive RIPK3-dependent astrocyte activation*

215 Given the strong representation of DAMP signaling in our transcriptomic analysis, we  
216 questioned whether factors released from dying neurons were important for driving RIPK3-  
217 mediated astrocyte activation. To test this, we treated differentiated SH-SY5Y neuroblastoma  
218 cells, a commonly used model of catecholaminergic neurons<sup>43</sup>, with the toxic MPTP metabolite  
219 MPP<sup>+</sup> (5mM) for 24 hours, which resulted in around 50% cell death (Supplemental Figure 3A).  
220 We harvested the conditioned media (NCM) from these cells, which contained DAMPs and  
221 other factors released from dying SH-SY5Y cells, and added it to primary human midbrain  
222 astrocyte cultures at a ratio of 1:1 with normal astrocyte culture media (Figure 5A). NCM-  
223 treated astrocytes were also treated with the RIPK3 inhibitor GSK872 or DMSO vehicle. qRT-  
224 PCR analysis following 24 hours of stimulation under these conditions revealed robust  
225 induction of genes associated with inflammatory activation in midbrain astrocyte cultures  
226 treated with NCM derived from MPP<sup>+</sup>-treated SH-SY5Y cultures, hereafter referred to as MPP<sup>+</sup>  
227 NCM (Figure 5B). However, pharmacologic inhibition of RIPK3 signaling in astrocytes largely  
228 prevented this effect.

229 After these observations, we recognized that our NCM preparations may have  
230 contained debris and floating “corpses” from dead SH-SY5Y cells. To assess whether soluble  
231 factors or dead cell-associated material was the primary driver of RIPK3-dependent astrocyte  
232 activation in our experiments, we carefully fractionated NCM samples to pellet out cellular  
233 material from soluble factors in the media. Application of either clarified supernatant (Figure

234 5C) or resuspended pellet material (Figure 5D) from MPP<sup>+</sup>-treated SH-SY5Y cells to midbrain  
235 astrocyte cultures revealed that clarified supernatants stimulated expression of many  
236 inflammatory genes in astrocytes in a largely RIPK3-dependent manner. In contrast, pellet-  
237 derived material was only minimally stimulatory, and this stimulation was RIPK3-independent.  
238 We also confirmed that exposure to residual MPP<sup>+</sup> in NCM was not the primary driver of  
239 astrocyte activation, as direct application of MPP<sup>+</sup> to midbrain astrocyte cultures did not result  
240 in either cell death or upregulation of inflammatory gene expression (Supplemental Figure 3B-  
241 C).

242 We next wanted to confirm that inflammatory gene expression in our system  
243 corresponded to a functional readout of astrocyte activation. We thus assessed whether  
244 exposure to dying neuron-derived factors would confer neurotoxic activity to astrocytes. We  
245 first treated human midbrain astrocytes for 24 hours with MPP<sup>+</sup> NCM with or without RIPK3  
246 inhibitor (and respective controls), then washed the cells and replaced the astrocyte medium to  
247 remove residual MPP<sup>+</sup>. We then cultured astrocytes for an additional 24h and collected their  
248 conditioned media (ACM), which was then added to fresh cultures of SH-SY5Y cells at a 1:1  
249 ratio with normal SH-SY5Y media (Figure 5E). We confirmed that astrocytes maintained  
250 transcriptional activation for at least 24 hours following this wash step, confirming that  
251 astrocytes remain activated after removal of MPP<sup>+</sup> NCM in this paradigm (Supplemental Figure  
252 4). ACM derived from MPP<sup>+</sup> NCM-treated astrocytes induced around 80% cell death in fresh  
253 SH-SY5Y cultures after 24 hours, while this neurotoxic activity was completely abrogated when  
254 astrocytic RIPK3 signaling was inhibited (Figure 5F). Together, these data show that soluble  
255 factors released from dying neuron-like cells are sufficient to induce inflammatory transcription  
256 and neurotoxic activity in midbrain astrocytes and that this process requires, to a large degree,  
257 cell-intrinsic RIPK3 activity within astrocytes.

258

### 259 *DAMP signaling via RAGE drives inflammatory activation in midbrain astrocytes*

260 We next sought to more precisely identify specific DAMP signals that stimulate midbrain  
261 astrocyte activation. Our transcriptomic analysis revealed that both HMGB1 and S100 family  
262 signaling were highly enriched in an astrocytic RIPK3-dependent manner in the midbrain  
263 following MPTP treatment. As both of these DAMPs stimulate a common receptor, RAGE, we  
264 assessed whether RAGE was required for astrocyte activation following exposure to MPP<sup>+</sup>  
265 NCM. We thus treated human midbrain astrocyte cultures with MPP<sup>+</sup> or control NCM, along  
266 with the RAGE inhibitor FPS-ZM1 for 24 hours and performed qRT-PCR profiling (Figure 6A).  
267 Blockade of RAGE in astrocytes substantially reduced MPP<sup>+</sup> NCM-induced transcriptional  
268 activation, effectively preventing upregulation of 6 out of 11 astrocyte activation-associated  
269 transcripts (Figure 6B). Based on these findings, we confirmed that the RAGE ligand HMGB1  
270 was, in fact, released by SH-SY5Y cells following induction of cell death by MPP<sup>+</sup> (Figure 6C).  
271 We also observed significant accumulation of HMGB1 protein in midbrain homogenates of  
272 mice treated with MPTP (Figure 6D), confirming that induction of dopaminergic cell death  
273 results in the release of RAGE ligands *in vivo*. To assess whether RAGE ligands induced  
274 astrocyte activation in a RIPK3-dependent manner, we next treated primary midbrain



275 astrocytes with recombinant DAMPs and profiled gene expression. Strikingly, we observed that  
276 stimulation of murine midbrain astrocytes with HMGB1 induced robust transcriptional activation  
277 that was blocked in the presence of GSK 872. As a complimentary approach, we also  
278 generated midbrain astrocyte cultures from *Ripk3*<sup>-/-</sup> mice (and heterozygous littermate controls)  
279 and stimulated with RAGE ligands. Treatment with either HMGB1 (Figure 6F) or S100β (Figure  
280 6G) induced inflammatory transcript expression in control but not *Ripk3*<sup>-/-</sup> cultures. Together,  
281 these data suggest that dying neurons release DAMPs that induce inflammatory astrocyte  
282 activation through activation of astrocytic RAGE, which in turn drives transcription via RIPK3  
283 signaling.

284

285 *Activation of RIPK3 by DAMP signaling drives pathogenic functional changes in midbrain*  
286 *astrocytes*

287 To confirm that the transcriptional effects of DAMP signaling impacted astrocyte  
288 function, we collected astrocyte conditioned media (ACM) from astrocytes treated for 24h with  
289 MPP<sup>+</sup> NCM with or without RAGE inhibitor (and respective controls) and applied the ACM to  
290 fresh cultures of SH-SY5Y cells (Figure 7A). ACM derived from MPP<sup>+</sup> NCM-treated astrocytes  
291 induced significant cell death in fresh SH-SY5Y cultures, while this neurotoxic activity was  
292 completely abrogated when astrocytic RAGE signaling was inhibited (Figure 7B). We also  
293 observed conferral of neurotoxic activity following direct stimulation of astrocytes with  
294 recombinant DAMPs (Figure 7C), including HMGB1 (Figure 7D) and S100β (Figure 7E).  
295 However, this neurotoxic activity was also abrogated when RIPK3 signaling was blocked,  
296 further supporting a role for a RAGE-RIPK3 axis in promoting neurotoxic astrocyte activation.  
297 This neurotoxic activity was not due to residual recombinant DAMPs in ACM, as direct  
298 application of either DAMP ligand to SH-SY5Y cells did not result in cell death (Supplemental  
299 Figure 5). As previous work has shown that neurotoxic astrocytes downregulated key  
300 homeostatic functions such as phagocytosis<sup>14,36</sup>, we also exposed midbrain astrocyte cultures  
301 to labeled debris generated from SH-SY5Y cells and measured phagocytic uptake of debris via  
302 flow cytometry (Figure 7F). Direct stimulation of astrocytes with HMGB1 resulted in a  
303 significant reduction in uptake of CFSE-labeled debris, while this suppression of phagocytic  
304 function was blocked in the presence of a RIPK3 inhibitor (Figure 7G-H). We also observed  
305 that MPP<sup>+</sup> NCM similarly reduced astrocytic phagocytosis in a RIPK3-dependent fashion  
306 (Figure 7I). These data further support the notion that DAMPs emanating from dying neurons  
307 alter astrocytic function via activation of RIPK3 signaling.

308

## 309 Discussion

310 Our study defines a previously unknown role for neuronal DAMPs in promoting  
311 neurotoxic astrocyte activation. This effect was mediated by RIPK3-mediated transcriptional  
312 activation, an effect that occurred independently of the necroptotic executioner protein MLKL.  
313 Mechanistically, we found that astrocytic RAGE signaling was required for astrocyte activation  
314 downstream of DAMP exposure, and this RAGE/RIPK3 signaling axis promoted inflammatory  
315 transcription and neurotoxic functional activity. Intriguingly, these results suggest that neuronal  
316 death, itself, potentiates a feed-forward process of astrocyte activation and further neuronal  
317 cell death. These findings highlight an important mechanism of neuron-glia crosstalk in the  
318 pathogenesis of neurodegeneration.

319 DAMPs have previously been implicated as drivers of inflammation in a broad variety of  
320 disorders, including neurodegeneration, ischemic stroke, autoimmunity, cardiovascular  
321 disease, and others<sup>44-55</sup>. RAGE ligands, in particular, have been associated with  
322 neurodegenerative disease and have been the target of preclinical therapeutic development.  
323 For example, S100 $\beta$  levels in serum and cerebrospinal fluid (CSF) has been shown to  
324 correlate with disease severity in Parkinson's disease<sup>27,56</sup>. Mice deficient in S100 $\beta$  are also  
325 resistant to MPTP-driven neurodegeneration<sup>27</sup>, consistent with a role for this molecule in  
326 perpetuating neuronal cell death. Similarly, antibody-mediated neutralization of HMGB1 has  
327 been shown to attenuate glial cell activation and prevent neuron loss in models of both  
328 Alzheimer's disease and Parkinson's disease<sup>26,57</sup>. Despite these findings, other groups have  
329 also described neuroprotective functions for RAGE ligands<sup>58</sup>, including stimulation of  
330 neurotrophic growth factor expression in amyotrophic lateral sclerosis<sup>59</sup>, suppression of  
331 amyloidosis<sup>60</sup>, and direct anti-apoptotic effects in neurons<sup>61,62</sup>. These complex effects appear  
332 to be highly context-dependent, differing by cell type, disease state, and even DAMP  
333 concentration<sup>61,63,64</sup>. Our data support a pathogenic role for RAGE signaling in the promotion of  
334 neurotoxic astrocyte activation.

335 Astrocytes express RAGE and other DAMP sensors, although cell type-specific  
336 functions for DAMP signaling in astrocytes have not been thoroughly studied<sup>65</sup>. Existing  
337 studies suggest that astrocytic RAGE signaling is pathogenic, on balance<sup>66-68</sup>. In Huntington's  
338 disease, RAGE-positive astrocytes have been shown to have high levels of nuclear NF- $\kappa$ B<sup>67</sup>,  
339 consistent with a role for this pathway in promoting inflammatory astrocyte activation.  
340 Diminished levels of HMGB1 following berberine treatment was also correlated with diminished  
341 astrocyte activation in a model of sepsis<sup>69</sup>. Astrocytes are also major sources of RAGE ligands,  
342 particularly S100 $\beta$ , and much work to date has focused on autocrine RAGE signaling in  
343 astrocytes as a result<sup>70-72</sup>. We took advantage of the MPTP model, which induces death  
344 selectively in neurons but not astrocytes<sup>73</sup>, as well as serial culture systems to more directly  
345 assess the impact of paracrine RAGE signaling on astrocyte activation and function. Our study  
346 suggests that DAMPs released from dying neurons potently induce inflammatory astrocyte  
347 activation via RAGE, driving neurotoxic activation and perpetuating further neuronal cell death.  
348 These findings identify RAGE as a promising target for modulating astrocytic responses to  
349 neuronal cell death during neurodegenerative disease.

350 RIPK3 signaling has previously been shown to drive pathogenic neuroinflammation and  
351 neuronal cell death in several models of neurological disorders<sup>14,15,74-77</sup>. While many studies  
352 have reported neuronal necroptosis as a driver of neurodegeneration, we and others have  
353 described necroptosis-independent functions for this kinase in the coordination of  
354 neuroinflammation<sup>12-18</sup>. To date, RIPK3 signaling in astrocytes has received relatively little  
355 attention. Our findings here suggest that DAMP signaling activates astrocytic RIPK3 via RAGE  
356 signaling, which drives an inflammatory transcriptional program, even in the absence of MLKL.  
357 These data suggest that astrocytic RAGE signaling does not induce inflammation via  
358 necroptosis, consistent with our prior work showing necroptosis-independent RIPK3 signaling  
359 in astrocytes exposed to fibrillar  $\alpha$ -synuclein<sup>14</sup>.

360 Future work will be needed to define the signaling events that mediate RAGE-  
361 dependent RIPK3 activation. A recent study demonstrated co-immunoprecipitation of RIPK3  
362 with RAGE in an endothelial cell line following stimulation with TNF- $\alpha$ <sup>78</sup>, but the nature of this  
363 interaction and whether it happens under natural conditions *in vivo* remains to be established.  
364 While some studies have observed RIPK3 activation downstream of HMGB1<sup>79,80</sup>, these effects  
365 may have been mediated by non-RAGE HMGB1 receptors such as TLR4, which is known to  
366 stimulate RIPK3 via its adaptor molecule TRIF<sup>81,82</sup>. Both RAGE and RIPK3 signaling appear to  
367 converge on the potent activation of NF- $\kappa$ B<sup>38,83-92</sup>, which may provide clues concerning their  
368 potential molecular interactions. In any event, delineating the molecular events that promote  
369 pathogenic astrocyte activation downstream of DAMP signaling will likely be required to  
370 effectively target this pathway for future therapeutic development.

371

## 372 Acknowledgements

373 The authors thank Drs. Noriko Goldsmith and Jessica Shivas for assistance with  
374 confocal imaging in the Human Genetics Institute of New Jersey Imaging Core Facility. We  
375 also thank Eric Chiles and Dr. Xiaoyang Su for assistance with LC/MS. LC/MS data were  
376 generated by the Rutgers Cancer Institute of New Jersey Metabolomics Shared Resource,  
377 supported, in part, with funding from NCI-CCSG P30CA072720-5923. Some figure elements  
378 were created with Biorender.com.

379 This work was supported by a research grant from the American Parkinson's Disease  
380 Association, NIH R01 NS120895, and startup funds from Rutgers University (all to BPD), as  
381 well as R00 MH112855 (to RH). NPC was supported by F31 NS124242. WRE was supported  
382 by T32 AA028254. DA was supported by fellowships from the Louis Stokes Alliance for  
383 Minority Participation (LSAMP) program.

384

## 385 Author Contributions

386 Conceptualization: NPC, BPD; Investigation: NPC, ED, WRE, MN, MM, DA, ML, TC,  
387 CA, BPD; Analysis: NPC, ED, MM, ML, TC, BPD; Resources: AWK, RH, BPD; Writing –

388 Original Draft: NPC, BPD; Writing – Review and Editing: NPC, ED, TC, CA, BPD; Supervision:  
389 CA, AWK, RH, BPD; Funding Acquisition: RH, BPD.

390

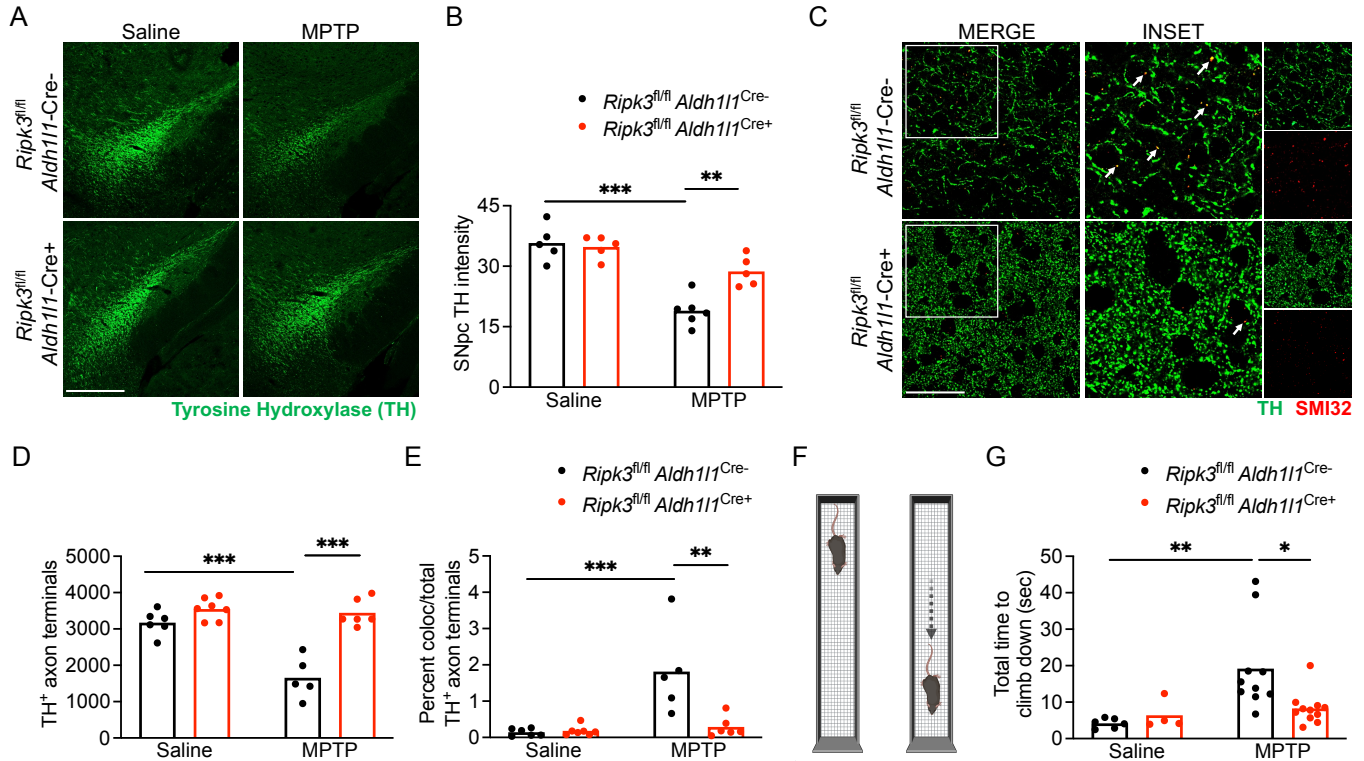
391 Competing Interests

392       The authors declare no competing interests.

393

394

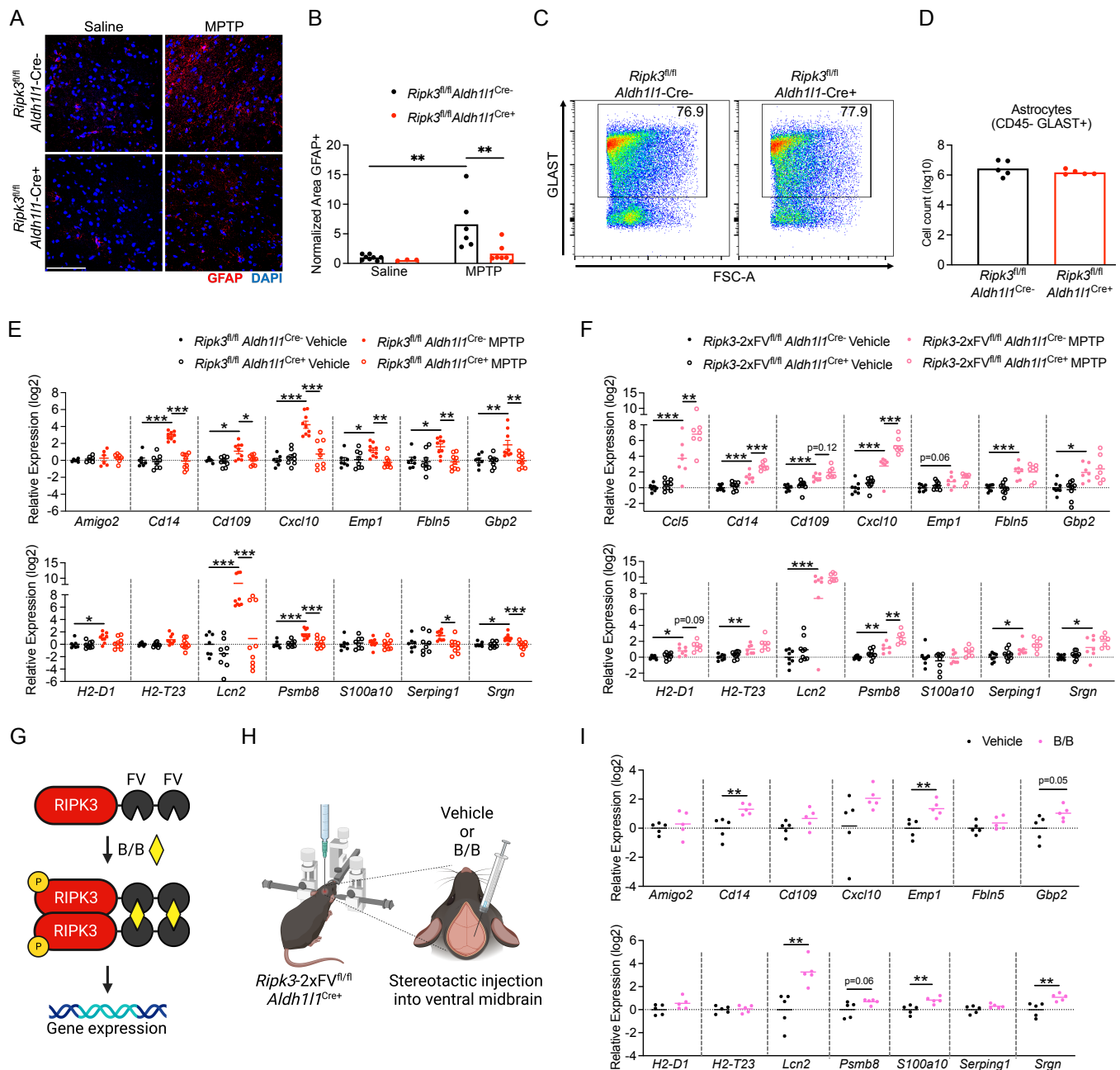
## Figures



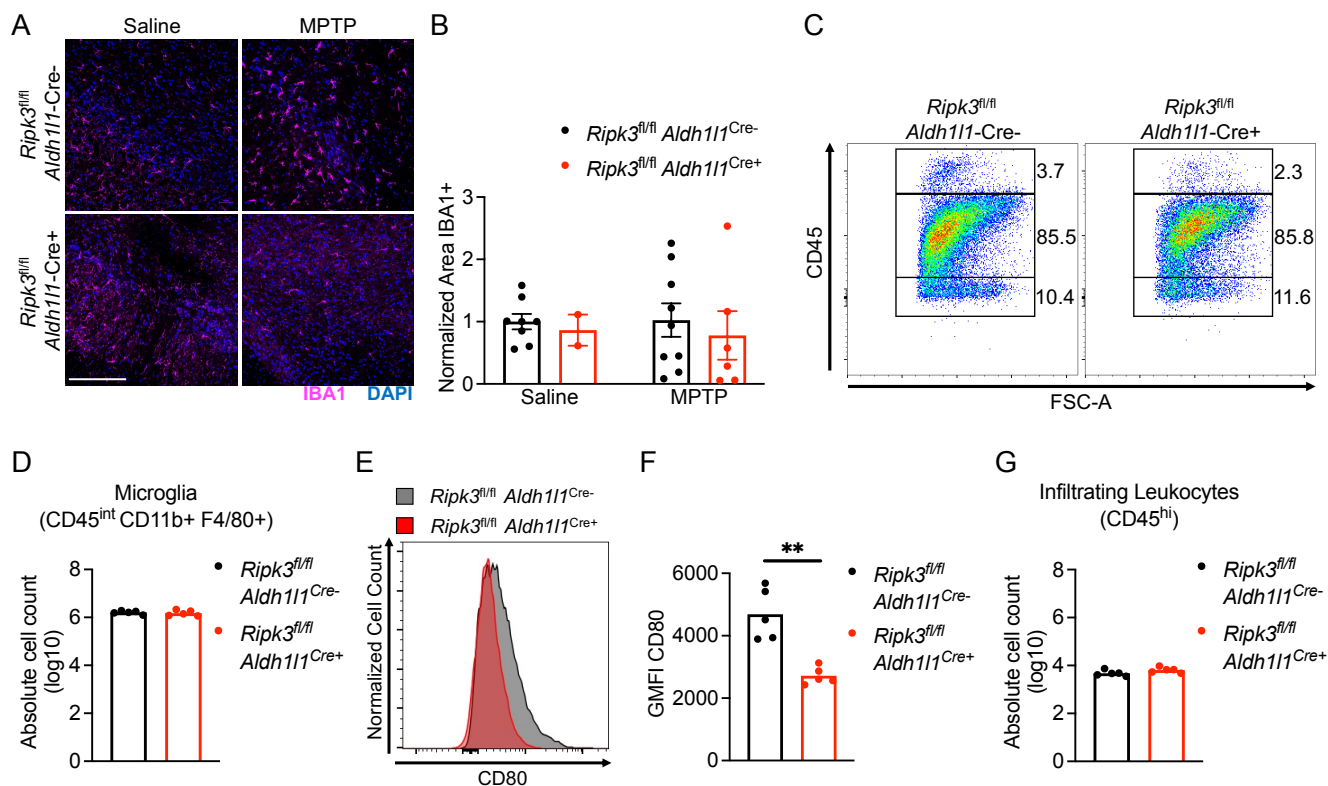
396

397

398 **Figure 1. Astrocytic RIPK3 signaling promotes pathogenesis in the MPTP model of**  
 399 **Parkinson's disease. (A-B)** IHC analysis of tyrosine hydroxylase (TH) staining in the  
 400 substantia nigra pars compacta (SNpc) in indicated genotypes 7 days following either saline or  
 401 MPTP treatment (scale bar = 200  $\mu$ m). **(C)** IHC analysis of TH<sup>+</sup> axons with colabeling with the  
 402 damaged axon marker SMI-32 in the striatum in indicated genotypes 7 days following either  
 403 saline or MPTP treatment (scale bar = 20  $\mu$ m). **(F)** Schematic diagram for the vertical grid test.  
 404 **(G)** Behavioral performance in the vertical grid test 6 days after injection with MPTP or saline.  
 405 \* $p < 0.05$ , \*\* $p < 0.01$ , \*\*\* $p < 0.001$ . See also Figure S1.



406 **Figure 2. RIPK3 drives inflammatory transcriptional activation but not proliferation in**  
 407 **midbrain astrocytes. (A-B)** IHC analysis of GFAP staining in the substantia nigra pars compacta  
 408 (SNpc) in indicated genotypes 3 days post-MPTP treatment (scale bar = 200  $\mu$ m). **(C-D)** Flow  
 409 cytometric analysis of GLAST+ astrocytes in midbrain homogenates derived from indicated  
 410 genotypes 3 days post-MPTP treatment. **(E-F)** qRT-PCR analysis of indicated genes in midbrain  
 411 homogenates derived from astrocyte-specific *Ripk3* knockouts **(E)** or astrocyte-specific *Ripk3*  
 412 overexpressing **(F)** mice 3 days post-MPTP treatment. **(G-H)** Schematic of inducible RIPK3  
 413 activation system **(G)** and stereotactic delivery of dimerization drug into the ventral midbrain **(H)**. **(I)**  
 414 qRT-PCR analysis of indicated genes in midbrain homogenates derived from *Ripk3-2xFV<sup>fl/fl</sup>*  
 415 *Aldh111-Cre+* mice 24 hours following administration of B/B homodimerizer or vehicle control.  
 416 \* $p < 0.05$ , \*\* $p < 0.01$ , \*\*\* $p < 0.001$ . See also Figure S2.



418

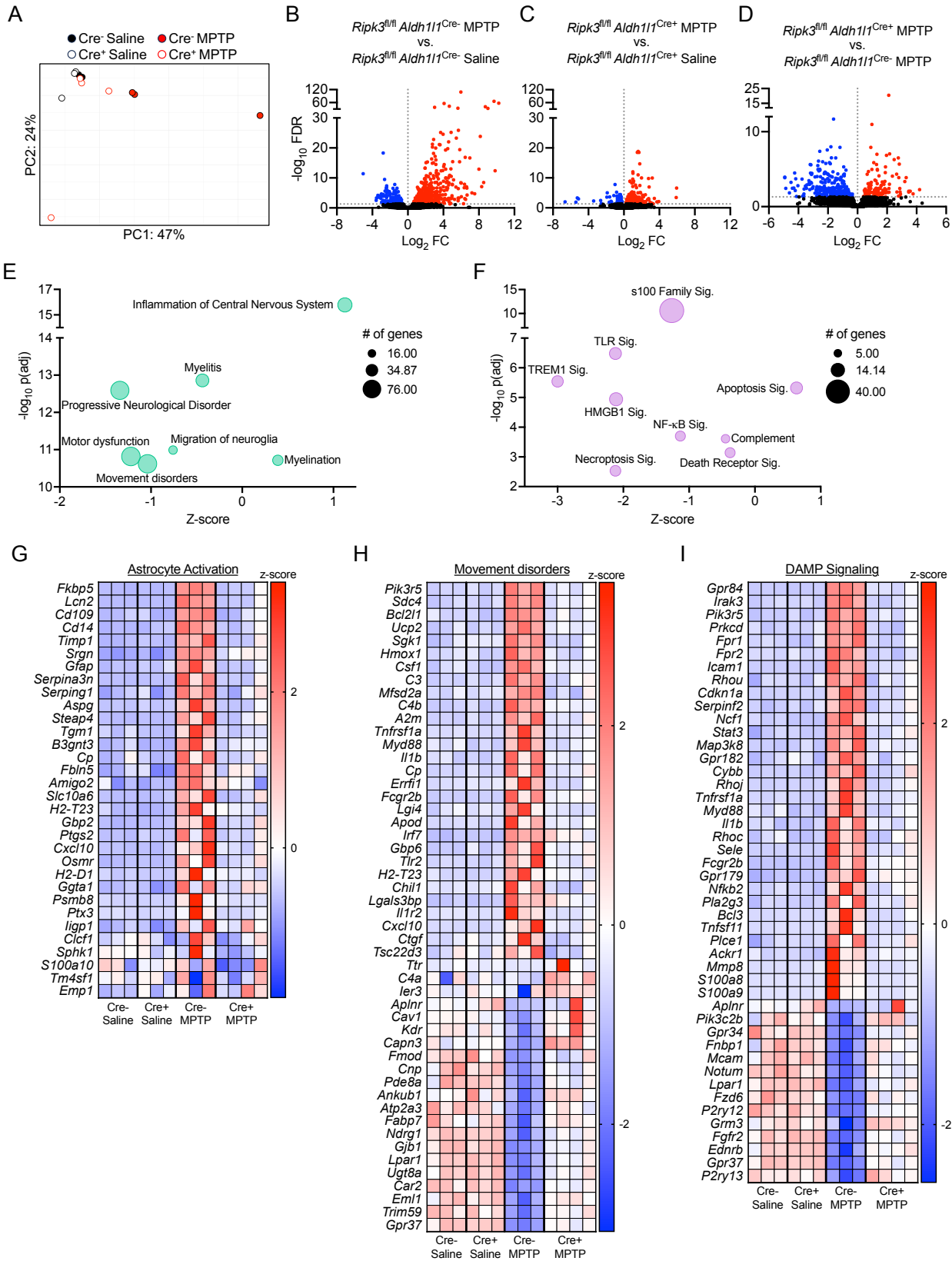
419

420

421

422 **Figure 3. Astrocytic RIPK3 signaling has minimal impact on microgliosis in the MPTP**  
 423 **model. (A-B)** IHC analysis of IBA1 staining in the substantia nigra pars compacta (SNpc) in  
 424 indicated genotypes 3 days post-MPTP treatment (scale bar = 200  $\mu$ m). **(C)** Representative  
 425 flow cytometric plot depicting leukocyte populations in midbrain homogenates derived from  
 426 indicated genotypes 3 days pos-MPTP treatment. **(D)** Quantification of absolute numbers of  
 427 microglia derived from flow cytometric analysis. **(E-F)** Representative histogram **(E)** and  
 428 quantification of geometric mean fluorescence intensity (GMFI) **(F)** derived from analysis of  
 429 CD80 expression on microglial populations in **(D)**. **(G)** Quantification of absolute numbers of  
 430 CD45<sup>hi</sup> leukocytes derived from flow cytometric analysis. \*\*p < 0.01

431



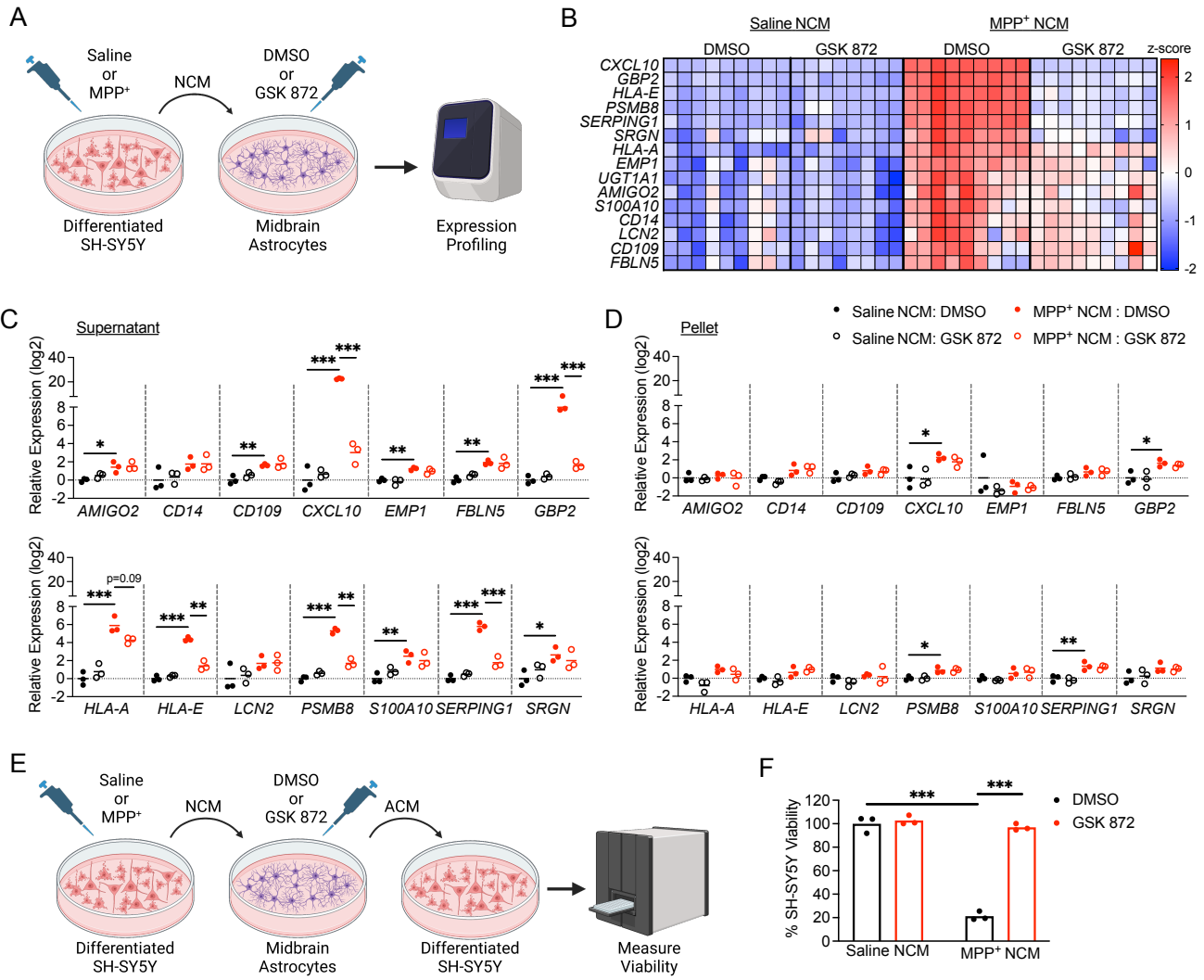
432

433



434 **Figure 4. Astrocytic RIPK3 activation drives a transcriptomic state associated with**  
435 ***inflammation and neurodegeneration in the midbrain.*** (A-I) Midbrains were harvested from  
436 mice of indicated genotypes 3 days post-treatment with MPTP or saline and subjected to bulk  
437 RNA-seq. (A) Principal component analysis demonstrating separation of treatment groups and  
438 genotypes in the RNA-seq dataset. (B-D) Volcano plots showing differentially expressed genes  
439 derived from indicated comparisons. Data points in red are genes exhibiting upregulated  
440 expression, while those in blue exhibit downregulated expression. Genes with an FDR <0.05  
441 were considered significant. (E-F) Bubble plots showing selected significantly enriched disease  
442 and function terms (E) or canonical pathways (F) derived from Ingenuity Pathway Analysis  
443 comparing Cre- vs. Cre+ MPTP-treated groups. (G-I) Heatmaps showing significantly  
444 differentially expressed genes for selected pathways.

445

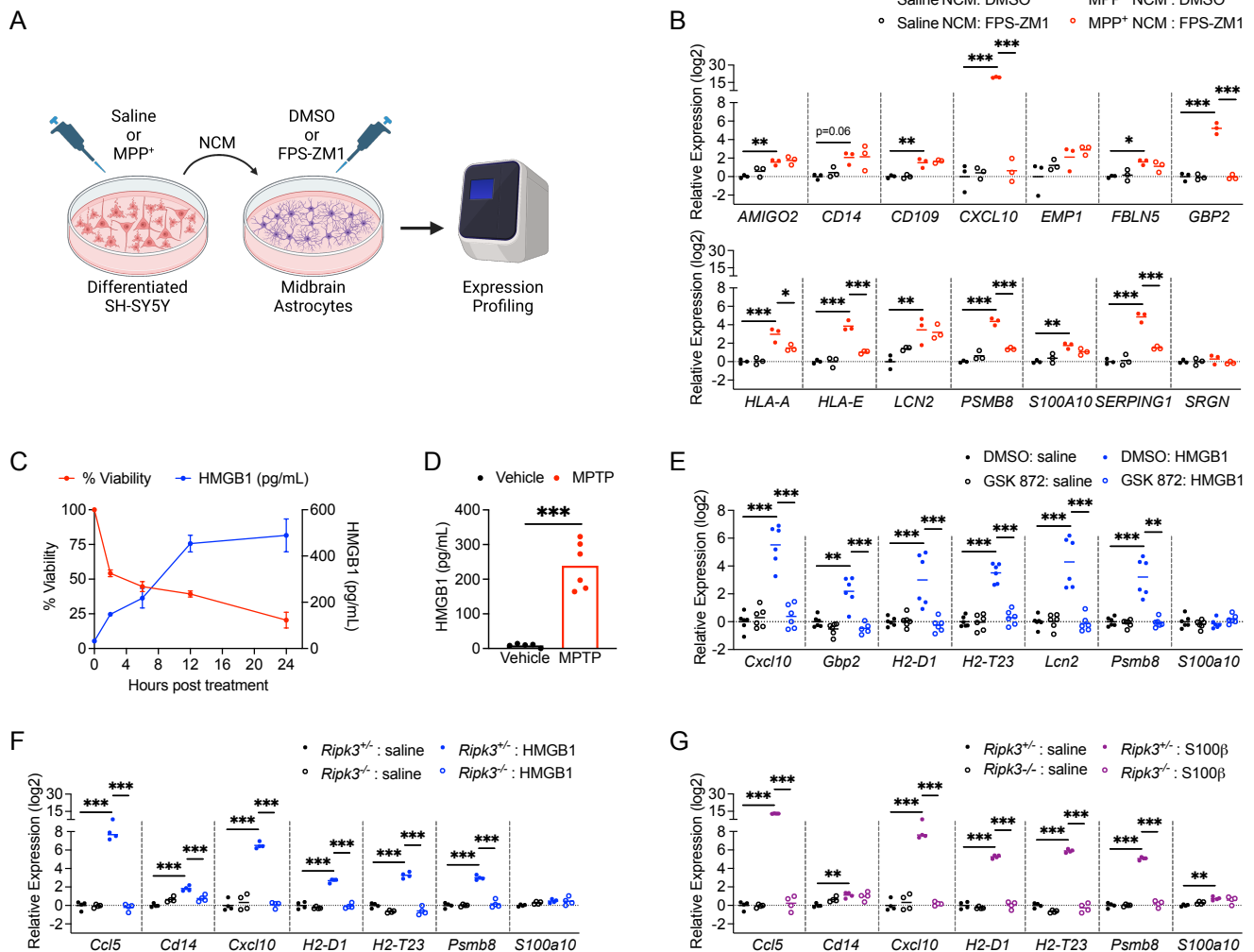


446

447 **Figure 5. Secreted factors from dying neurons drive RIPK3-dependent astrocyte**  
 448 **activation. (A)** Schematic of experimental design for DAMP transfer experiments.

449 Differentiated SH-SY5Y cells were treated with MPP<sup>+</sup> or saline for 24h and media (NCM) was  
 450 then transferred to cultures of primary human midbrain astrocytes. Astrocytes were treated  
 451 with NCM in the presence of GSK 872 or control for 24h prior to qRT-PCR profiling. **(B)**  
 452 Heatmap showing expression of astrocyte activation-associated genes in astrocyte cultures  
 453 treated as in **(A)**. **(C-D)** qRT-PCR profiling of indicated genes in astrocytes treated for 24h with  
 454 clarified NCM supernatants **(C)** or pelleted SH-SY5Y debris **(D)**. **(E)** Schematic of experimental  
 455 design for neurotoxicity assay. Astrocytes were treated with NCM as in **(A)** for 24h. Astrocytes  
 456 were then washed and media replaced for another 24h. This new astrocyte conditioned  
 457 medium (ACM) was then transferred to fresh SH-SY5Y cells for cell viability measurement. **(F)**  
 458 Cell Titer Glo analysis of SH-SY5Y viability 24h following treatment with ACM derived from  
 459 indicated conditions. \*p<0.05, \*\*p < 0.01, \*\*\*p < 0.001. See also Figures S3 and S4.

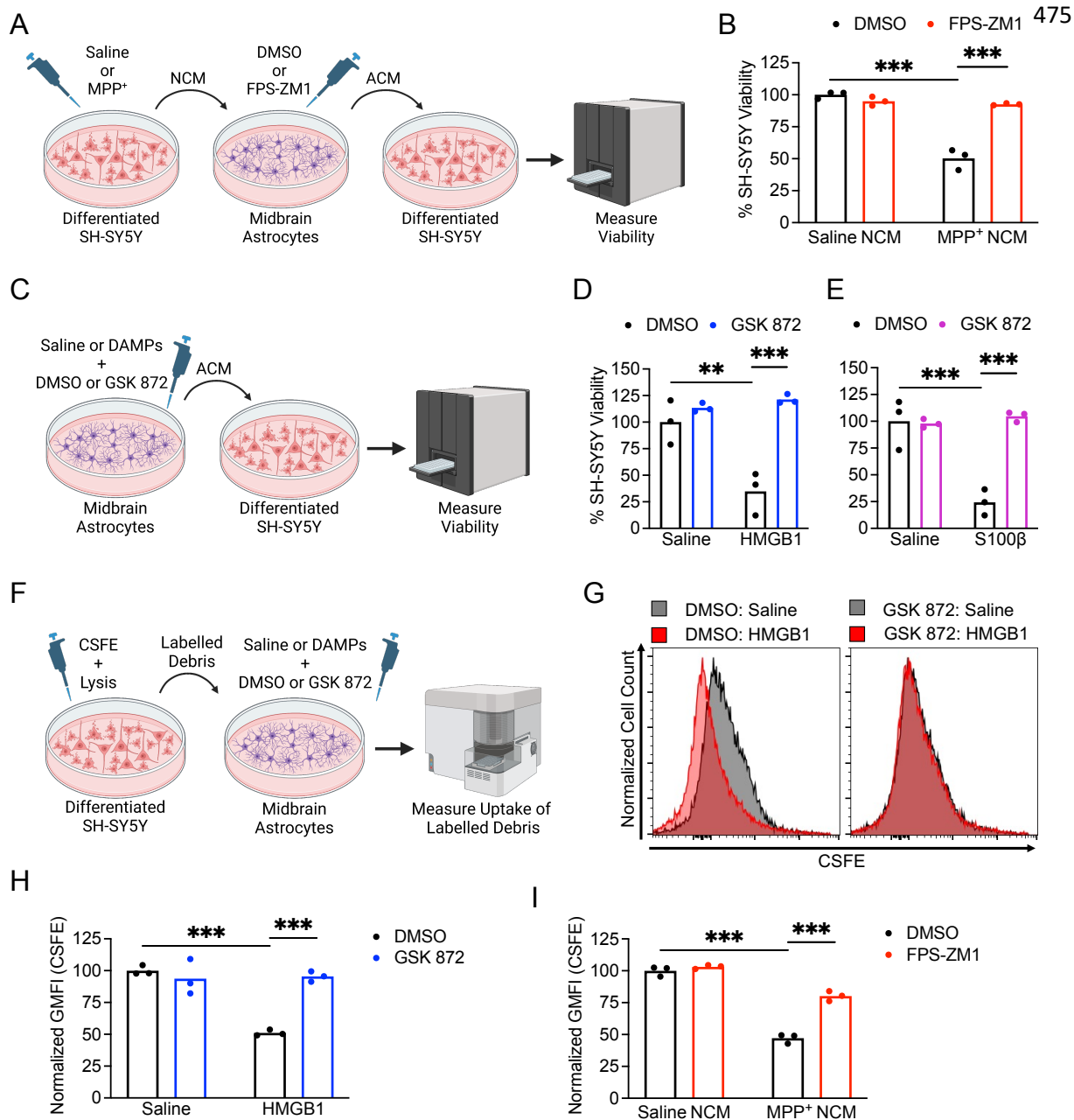
460



461

462 **Figure 6. DAMP signaling via RAGE drives inflammatory activation in midbrain**  
 463 **astrocytes. (A)** Schematic of experimental design for DAMP transfer experiments.  
 464 Differentiated SH-SY5Y cells were treated with MPP<sup>+</sup> or saline for 24h and media (NCM) was  
 465 then transferred to cultures of primary human midbrain astrocytes. Astrocytes were treated  
 466 with NCM in the presence of FPS-ZM1 or control for 24h prior to qRT-PCR profiling. **(B)** qRT-  
 467 PCR profiling of indicated genes in astrocytes treated for 24h with NCM derived from indicated  
 468 conditions. **(C-D)** ELISA analysis of HMGB1 protein levels in supernatants of SH-SY5Y cells  
 469 treated with MPP<sup>+</sup> **(C)** or midbrain homogenates from WT mice 3 days post-MPTP treatment  
 470 **(D)** n=4-8 replicates per time point in **(C)**. **(E-G)** qRT-PCR analysis of indicated genes in WT  
 471 murine midbrain astrocytes **(E)** or midbrain astrocytes derived from indicated genotypes **(F-G)**  
 472 24h following treatment with recombinant HMGB1 **(E-F)** or S100β **(G)**. \*p<0.05, \*\*p < 0.01, \*\*\*p  
 473 < 0.001.

474



476 **Figure 7. Activation of RIPK3 by DAMP signaling drives pathogenic functional changes**  
 477 **in midbrain astrocytes. (A)** Schematic of experimental design for neurotoxicity experiments.  
 478 Differentiated SH-SY5Y cells were treated with MPP<sup>+</sup> or saline for 24h and media (NCM) was  
 479 then transferred to cultures of primary human midbrain astrocytes. Astrocytes were treated  
 480 with NCM in the presence of FPS-ZM1 or control for 24h. Astrocytes were then washed and  
 481 media replaced for another 24h. This new astrocyte conditioned medium (ACM) was then  
 482 transferred to fresh SH-SY5Y cells for cell viability measurement. **(B)** Cell Titer Glo analysis of  
 483 SH-SY5Y viability 24h following treatment with ACM derived from indicated conditions. **(C)**  
 484 Schematic showing treatment of primary human midbrain astrocytes with recombinant DAMPs  
 485 for 24h prior to transfer of ACM to SH-SY5Y cultures and measurement of cell viability. **(D)** Cell

486 Titer Glo analysis of SH-SY5Y viability 24h following treatment with ACM derived from  
487 indicated conditions. **(F)** Schematic showing generation and transfer of CSFE-labeled neuronal  
488 debris to midbrain astrocytes treated with recombinant DAMPs with or without GSK 872.  
489 Astrocytes were cultured in the presence of labelled debris for 24h and then CSFE  
490 internalization was measured via flow cytometry. **(G-H)** Representative histograms **(G)** and  
491 quantification of GMFI **(H)** of CSFE signal in astrocytes treated as in **(F)**. **(I)** GMFI of CSFE  
492 internalization in astrocytes treated as in **(F)** but with NCM rather than recombinant DAMPs  
493 and FPS-ZM1 rather than GSK 872. \*\*p < 0.01, \*\*\*p < 0.001. See also Figure S5.

494

495

## 496 **Methods**

497

### 498 **Mouse lines**

499 Mice were bred and housed under specific-pathogen free conditions in Nelson Biological Laboratories  
500 at Rutgers University. *Ripk3*<sup>-/-</sup> and *Ripk3*<sup>fl/fl</sup> mouse lines were generously provided by Genentech, Inc.  
501 *Mik*<sup>+/93</sup> and *Ripk3-2xFV*<sup>fl/fl12</sup> lines were provided by Andrew Oberst (University of Washington). *Aldh111-*  
502 *Cre/ERT2* mice were obtained from Jackson Laboratories (Line 031008) and all animals expressing this  
503 transgene were treated for five days with 60 mg/kg tamoxifen (Sigma-Aldrich, T5648) in sunflower oil  
504 (Sigma-Aldrich, S5007) (i.p.) at least one week prior to further experimentation. All genotyping was  
505 performed in house using ear punch tissue lysed overnight in DirectPCR Lysis Reagent (Viagen, 102-T)  
506 and Proteinase K (Sigma, #3115828001). Sequences for genotyping primers are listed in the  
507 Supplementary Table S1. PCR bands were visualized on 2% agarose (VWR, 97062) in TBE (VWR,  
508 E442) and stained in Diamond Nucleic Acid Stain (Promega, H1181). All experiments were performed  
509 in 8-12 week old animals, following protocols approved by the Rutgers University Institutional Animal  
510 Care and Use Committee (IACUC). All MPTP experiments were performed in male animals, as female  
511 animals experience high rates of toxicity and mortality in this model<sup>29</sup>. Other experiments, including B/B  
512 homodimerizer administration and primary cell culture, used balanced groups of both male and female  
513 animals.

### 514 **MPTP model**

515 1-methyl-4-phenyl-1,2,3,6-tetrahydropyridine (MPTP) was administered at 20 mg/kg (i.p.) once per day  
516 for five days<sup>94</sup>. Animals were harvested three days following the final MPTP injection for gene  
517 expression and flow cytometry experiments. Animals were harvested seven days after the last injection  
518 for immunofluorescence (IF) and vertical grid maze studies.

### 519 **Tissue collection**

520 Mice were perfused transcardially with ice cold phosphate-buffered saline (PBS) followed by 4%  
521 paraformaldehyde (PFA) for IF experiments. Perfused brains were stored in 4% PFA overnight followed  
522 by 48 hours in 30% sucrose in PBS. For transcriptional and ELISA studies, mice were perfused with  
523 PBS and midbrain and/or striatal tissues were collected and homogenized for downstream analyses.

### 524 **Cell culture and treatment**

525 Primary human midbrain astrocytes (ScienCell Research Laboratories) were cultured in astrocyte  
526 media (ScienCell, 1801) supplemented with 2% heat-inactivated fetal bovine serum (FBS) (ScienCell,  
527 0010), astrocyte growth supplement (ScienCell, 1852), and penicillin/streptomycin (ScienCell, 0503).  
528 Cells from at least two distinct donors were used for all experiments. Human neuroblastoma SH-SY5Y  
529 cells (ATCC, CRL-2266) were cultured in DMEM medium (VWR, 0101-0500) supplemented with 10%  
530 FBS (Gemini Biosciences, 100-106), nonessential amino acids (Hyclone, SH30138.01), HEPES  
531 (Hyclone, 30237.01), penicillin/streptomycin (Gemini Biosciences, 400-110), and amphotericin B  
532 antifungal (Gemini Biosciences, 100-104). Differentiation and experimentation occurred in stocks  
533 having undergone less than 15 passages. SH-SY5Y neuroblastoma cells were differentiated into  
534 mature neuron-like cells by treating with retinoic acid (4 µg/mL; Sigma-Aldrich, R2625) and BDNF  
535 (25 ng/mL; Sigma-Aldrich, B3795) in low serum (2%) SH-SY5Y media. Differentiated SH-SY5Y cultures  
536 were used for experiments five to seven days post-differentiation. MPP<sup>+</sup> iodide (Sigma-Aldrich, D048)  
537 was formulated in water to a stock concentration of 500 mM. Recombinant HMGB1 (R&D Systems,

538 1690-HMB-050) and S100B (Human: R&D Systems, 1820-SB; Mouse: Novus Biologicals, NBP2-  
539 53070) were formulated according to manufacturer recommendations. For cell culture experiments, all  
540 recombinant DAMPs were used at a final concentration of 100 ng/mL for 24 h before collection of  
541 preconditioned media and cell lysates. GSK 872 was purchased from Millipore Sigma (530389). FPS-  
542 ZM1 was purchased from Sigma-Aldrich (55030). All inhibitors were solubilized in DMSO and used at a  
543 final concentration of 1  $\mu$ M.

#### 544 **Primary mouse astrocyte isolation and culture**

545 Primary mouse midbrain astrocytes were cultured from dissected midbrain tissues derived from mouse  
546 pups on postnatal day three (P3). Tissue was dissociated using Miltenyi Neural Dissociation Kit (T)  
547 following manufacturer's instructions (Miltenyi, 130-093-231). Midbrain astrocytes were cultured on  
548 fibronectin-coated flasks and non-astrocytic cells were removed via differential adhesion, as previously  
549 described<sup>95</sup>. Astrocytes were expanded in AM-a medium (ScienCell, 1831) supplemented with 10%  
550 FBS, Astrocyte Growth Supplement-animal (ScienCell, 1882) and Penicillin/Streptomycin Solution  
551 (ScienCell, 0503).

#### 552 **Cell viability test**

553 Cell viability was assessed with the CellTiter-Glo Luminescent Cell Viability Assay kit (Promega,  
554 G7573), according to the manufacturer's instructions. Luminescence signal was measured with a  
555 SpectraMax iD3 plate reader (Molecular Devices).

#### 556 **Phagocytosis assay**

557 Differentiated SH-SY5Y neuronal cells were labeled with BioTracker CSFE Cell Proliferation Kit  
558 (Millipore Sigma, SCT110) according to the manufacturer's protocol. Cell death was induced by  
559 exposure to TNF- $\alpha$  at 100 ng/mL and cycloheximide (Sigma-Aldrich, 66-81-9) at 100  $\mu$ g/mL for 24 h.  
560 Labelled cell debris was collected by centrifugation. Unlabeled neuronal debris was used as a staining  
561 control. To detect phagocytosis, CSFE-labeled neuronal debris was added to primary midbrain  
562 astrocyte cultures at a ratio of 1:100 for 24 h. Excess neuronal debris was washed away with PBS.  
563 Astrocytes were then harvested with cold 5 mM EDTA in PBS followed by scraping of adherent cells.  
564 Astrocytes were stained with Zombie NIR at 1:1000 in 1XPBS according to the manufacturer's protocol,  
565 followed by fixation in 1% PFA. Phagocytosed CSFE signal was detected using a Northern Lights flow  
566 cytometer (Cytek). Analysis was performed by FlowJo software (FlowJo LLC).

#### 567 **Immunofluorescence**

568 Brains were cryosectioned at 12  $\mu$ m per slice and mounted on a charged slide. Following thawing in a  
569 humidified chamber, tissues were incubated in blocking solution consisting of 5% goat serum (Gibco,  
570 16210) and 0.2% Triton X-100 for one hour at room temperature. Sections were then incubated with  
571 primary antibody diluted in blocking solution overnight at 4°C in a humidified chamber. Slides were then  
572 washed three times with PBS for 15 minutes followed by incubation in secondary antibody diluted in  
573 blocking solution for one hour at room temperature. Slides were washed three times to remove  
574 secondary antibody and were then stained with 4',6-diamidino-2-phenylindole (DAPI; Biotium, 40011)  
575 diluted in PBS for 20 minutes at room temperature, followed by another wash. Sections were cover-  
576 slipped with Prolong Diamond Antifade Mountant medium (Invitrogen, P36930). Slides were allowed to  
577 dry and images were acquired using Airyscan fluorescent confocal microscope (Carl Zeiss, LSM 800).

#### 578 **B/B homodimerizer and stereotactic injection**

579 B/B homodimerizer was purchased from Takara USA Inc. (AP20187) and was formulated according to  
580 manufacturer's recommendations. Buprenorphine extended-release (3.25mg/kg) was administered  
581 subcutaneously immediately prior to surgery. Mice were anaesthetized with isoflurane (4% induction,  
582 1% maintenance) and positioned on a heating pad while the head was fixed for stereotactic injection.  
583 Each animal received 500 nL of freshly formulated B/B homodimerizer or vehicle delivered by a glass  
584 pipette using a Programmable Nanoject III Nanoliter Injector (Drummond) unilaterally into the right  
585 ventral lateral midbrain (relative to bregma: coordinates A/P: -3.00mm, M/L: -1.20mm, D/V: -4.50mm).  
586 The scalp was sutured, and animals were allowed to recover for 24 h before transcriptional analyses.

### 587 **Quantitative real-time PCR**

588 Total RNA from homogenized midbrain tissues was extracted using Zymo Direct-zol RNA Miniprep kit,  
589 following manufacturer's instructions (Zymo, R2051). Total RNA from cultured cells was isolated using  
590 Qiagen RNeasy Mini Kit according to the manufacturer's protocol (Qiagen, 74106). RNA yield and  
591 quality of the samples were assessed using a NanoDrop spectrophotometer. cDNA was then  
592 synthesized with qScript cDNA Synthesis Kit (Quantabio, 95047), followed by qRT-PCR with SYBR  
593 Green Master Mix (Bio-Rad, 1725275). Cycle threshold (Ct) values were obtained using QuantStudio 5  
594 instrument (Applied Biosystems). Delta Ct was calculated as normalized to Ct values of the  
595 housekeeping gene 18S ( $Ct_{\text{Target}} - Ct_{18S} = \Delta Ct$ ). Z-scores were calculated to graph heatmaps. Primer  
596 sequences in our study are listed in Supplementary Table S2.

### 597 **Flow Cytometry**

598 After perfusing with ice-cold PBS, mouse midbrains were dissected and minced with a blade. Tissues  
599 were then further homogenized via 30 minute incubation in pre-warmed digestion buffer consisting of  
600 2% FBS, 1% glutamine, 1% non-essential amino acids, 1% penicillin/streptomycin/amphotericin, and  
601 1.5% HEPES, with 0.7U/mL collagenase VIII and 50U/mL DNase I on an orbital shaker. Triturated  
602 tissue homogenate was then passed through a 70  $\mu\text{m}$  cell strainer and centrifuged at 350 $\times g$  at 4°C for  
603 10 minutes to obtain a single-cell suspension. Cell gradient separation was then achieved by  
604 resuspending the pellet in 20% bovine-serum albumin (BSA) in DMEM followed by 20 minute  
605 centrifugation at 4°C. After removing the myelin layer, the cell gradient was disrupted by inverting in  
606 additional FACS buffer that consisted of 1mM EDTA in PBS with 1% BSA. Resuspended cells were  
607 then incubated in antibodies for 30 min at 4°C in the dark. After washing with cold FACS buffer, cold  
608 1% paraformaldehyde was then used to fix the cells. Data collection and analysis were performed using  
609 a Cytex Northern Lights Cytometer and FlowJo software. Data were normalized using standard  
610 counting beads (ThermoFisher, #C36950).

### 611 **HMGB1 enzyme-linked immunosorbent assay (ELISA)**

612 HMGB1 ELISA (Novus Biologicals, NBP2-62766) was performed following the manufacturer's protocol.

### 613 **Liquid chromatography-mass spectrometry (LC-MS)**

614 A single dosage of MPTP (40 mg/kg) was administered for LC-MS analysis of MPP<sup>+</sup> *in vivo*. Mice were  
615 transcidentally perfused with ice-cold PBS 90 min after MPTP injection. Whole brain tissues were then  
616 isolated and homogenized in CryoMill tubes containing cold 40:40:20 methanol:acetonitrile:water  
617 solution with 0.5% Formic Acid. Following a 10 min incubation on ice, tissue homogenates were then  
618 centrifuged in the cold room for 10 min for 16,000  $\times g$ . Supernatants were then transferred to a new  
619 collection tube. The final sample was then treated with 15%  $\text{NH}_4\text{HCO}_3$ . LC/MS was performed at the



620 Metabolomics Shared Resource Core Facility at the Rutgers Cancer Institute of New Jersey (New  
621 Brunswick, NJ).

622

### 623 **Behavioral assessment**

624 The vertical grid motor assessment task was adapted from previous work<sup>34</sup>. Briefly, mice were  
625 acclimated to the vertical grid apparatus 3 times a day for 2 consecutive days. On each day, each  
626 mouse was placed on the inside of the apparatus 3 cm from the top, facing upward, and was allowed to  
627 turn around and climb down. The trial was repeated whenever the mouse failed to climb down and/or  
628 turn around within 60 seconds. The same trials were repeated on the day following acclimation and  
629 video recorded for analysis.

### 630 **Bulk RNA sequencing**

631 Total RNA from midbrain tissues was extracted and assessed as described above. RNA samples were  
632 sent to Azenta (Piscataway, NJ) for library preparation and Next Generation Sequencing. RNA yield  
633 and sample quality were assessed with Qubit (Invitrogen) and TapeStation (Agilent). The Illumina  
634 HiSeq platform and 2 x 150-bp paired-end reads were used for the RNA sequencing. Initial analysis  
635 was processed by Azenta. The quality of raw RNA-seq data (FASTQ) files were evaluated using  
636 FASTQC. Sequence reads were trimmed to remove possible adapter sequences and nucleotides with  
637 poor quality using Trimmomatic v.0.36. Trimmed reads were then mapped to the mouse reference  
638 genome (GRCm38) available on ENSEMBL using the STAR aligner v.2.5.2b. Unique gene hit counts  
639 were calculated by using featureCounts from the Subread package v.1.5.2. The gene hit counts table  
640 was used for downstream differential expression analysis via DESeq2. Further statistical analysis was  
641 performed using R.

642

### 643 **Image analysis**

644 To quantify TH<sup>+</sup> and SMI32<sup>+</sup> puncta and co-localization, images were processed by Imaris software  
645 (Oxford Instruments, Bitplane 9.5). Object based co-localization was used with the “Coloc” feature. For  
646 TH<sup>+</sup> and SMI32<sup>+</sup> particles, the spot detection function was used to define particles by first creating  
647 ‘vesicles’ in each channel. Input intensity for threshold was chosen to best represent the signal for both  
648 channels. Colocalized particles were defined with the “classification” feature, where the distance  
649 between TH<sup>+</sup> and SMI32<sup>+</sup> particles within 1  $\mu$ m or less is considered co-localization. The percentage  
650 area and mean intensity of GFAP<sup>+</sup> and IBA1<sup>+</sup> signal were assessed using Fiji (ImageJ) software.

### 651 **Statistical analysis**

652 Statistical analysis was completed using GraphPad Prism 9 (GraphPad). Normally distributed data  
653 were analyzed using appropriate parametric tests: student’s t test (2-tailed) or two-way analysis of  
654 variance (ANOVA) with Tukey’s post hoc test used to determine significant differences between groups.  
655 A p value less than 0.05 was considered statistically significant. All data points represent biological  
656 replicates unless otherwise noted.

657

658

659

**References**

- 661 1. Gilhus, N.E., and Deuschl, G. (2019). Neuroinflammation - a common thread in  
662 neurological disorders. *Nat Rev Neurol* 15, 429-430. 10.1038/s41582-019-0227-8.
- 663 2. Boyd, R.J., Avramopoulos, D., Jantzie, L.L., and McCallion, A.S. (2022).  
664 Neuroinflammation represents a common theme amongst genetic and environmental  
665 risk factors for Alzheimer and Parkinson diseases. *J Neuroinflammation* 19, 223.  
666 10.1186/s12974-022-02584-x.
- 667 3. Giovannoni, F., and Quintana, F.J. (2020). The Role of Astrocytes in CNS Inflammation.  
668 *Trends Immunol* 41, 805-819. 10.1016/j.it.2020.07.007.
- 669 4. Endo, F., Kasai, A., Soto, J.S., Yu, X., Qu, Z., Hashimoto, H., Gradinaru, V., Kawaguchi,  
670 R., and Khakh, B.S. (2022). Molecular basis of astrocyte diversity and morphology  
671 across the CNS in health and disease. *Science* 378, eadc9020.  
672 10.1126/science.adc9020.
- 673 5. Patani, R., Hardingham, G.E., and Liddel, S.A. (2023). Functional roles of reactive  
674 astrocytes in neuroinflammation and neurodegeneration. *Nat Rev Neurol* 19, 395-409.  
675 10.1038/s41582-023-00822-1.
- 676 6. Escartin, C., Galea, E., Lakatos, A., O'Callaghan, J.P., Petzold, G.C., Serrano-Pozo, A.,  
677 Steinhauser, C., Volterra, A., Carmignoto, G., Agarwal, A., et al. (2021). Reactive  
678 astrocyte nomenclature, definitions, and future directions. *Nat Neurosci* 24, 312-325.  
679 10.1038/s41593-020-00783-4.
- 680 7. Brandebura, A.N., Paumier, A., Onur, T.S., and Allen, N.J. (2023). Astrocyte  
681 contribution to dysfunction, risk and progression in neurodegenerative disorders. *Nat*  
682 *Rev Neurosci* 24, 23-39. 10.1038/s41583-022-00641-1.
- 683 8. Angel, J.P., and Daniels, B.P. (2022). Paradoxical roles for programmed cell death  
684 signaling during viral infection of the central nervous system. *Curr Opin Neurobiol* 77,  
685 102629. 10.1016/j.conb.2022.102629.
- 686 9. Mangalmurti, A., and Lukens, J.R. (2022). How neurons die in Alzheimer's disease:  
687 Implications for neuroinflammation. *Curr Opin Neurobiol* 75, 102575.  
688 10.1016/j.conb.2022.102575.
- 689 10. Heckmann, B.L., Tummers, B., and Green, D.R. (2019). Crashing the computer:  
690 apoptosis vs. necroptosis in neuroinflammation. *Cell Death Differ* 26, 41-52.  
691 10.1038/s41418-018-0195-3.
- 692 11. Morgan, M.J., and Kim, Y.S. (2022). Roles of RIPK3 in necroptosis, cell signaling, and  
693 disease. *Exp Mol Med* 54, 1695-1704. 10.1038/s12276-022-00868-z.
- 694 12. Daniels, B.P., Snyder, A.G., Olsen, T.M., Orozco, S., Oguin, T.H., 3rd, Tait, S.W.G.,  
695 Martinez, J., Gale, M., Jr., Loo, Y.M., and Oberst, A. (2017). RIPK3 Restricts Viral  
696 Pathogenesis via Cell Death-Independent Neuroinflammation. *Cell* 169, 301-313 e311.  
697 10.1016/j.cell.2017.03.011.
- 698 13. Daniels, B.P., Kofman, S.B., Smith, J.R., Norris, G.T., Snyder, A.G., Kolb, J.P., Gao, X.,  
699 Locasale, J.W., Martinez, J., Gale, M., Jr., et al. (2019). The Nucleotide Sensor ZBP1  
700 and Kinase RIPK3 Induce the Enzyme IRG1 to Promote an Antiviral Metabolic State in  
701 Neurons. *Immunity* 50, 64-76 e64. 10.1016/j.immuni.2018.11.017.
- 702 14. Chou, T.W., Chang, N.P., Krishnagiri, M., Patel, A.P., Lindman, M., Angel, J.P., Kung,  
703 P.L., Atkins, C., and Daniels, B.P. (2021). Fibrillar alpha-synuclein induces neurotoxic  
704 astrocyte activation via RIP kinase signaling and NF-kappaB. *Cell Death Dis* 12, 756.  
705 10.1038/s41419-021-04049-0.

- 706 15. Wu, L., Chung, J.Y., Cao, T., Jin, G., Edmiston, W.J., 3rd, Hickman, S., Levy, E.S.,  
707 Whalen, J.A., Abrams, E.S.L., Degtarev, A., et al. (2021). Genetic inhibition of RIPK3  
708 ameliorates functional outcome in controlled cortical impact independent of necroptosis.  
709 *Cell Death Dis* 12, 1064. 10.1038/s41419-021-04333-z.
- 710 16. Guo, H., Koehler, H.S., Mocarski, E.S., and Dix, R.D. (2022). RIPK3 and caspase 8  
711 collaborate to limit herpes simplex encephalitis. *PLoS Pathog* 18, e1010857.  
712 10.1371/journal.ppat.1010857.
- 713 17. Cervantes, P.W., Martorelli Di Genova, B., Erazo Flores, B.J., and Knoll, L.J. (2021).  
714 RIPK3 Facilitates Host Resistance to Oral *Toxoplasma gondii* Infection. *Infect Immun*  
715 89. 10.1128/IAI.00021-21.
- 716 18. Preston, S.P., Allison, C.C., Schaefer, J., Clow, W., Bader, S.M., Collard, S., Forsyth,  
717 W.O., Clark, M.P., Garnham, A.L., Li-Wai-Suen, C.S.N., et al. (2023). A necroptosis-  
718 independent function of RIPK3 promotes immune dysfunction and prevents control of  
719 chronic LCMV infection. *Cell Death Dis* 14, 123. 10.1038/s41419-023-05635-0.
- 720 19. Gul-Hinc, S., Michno, A., Zysk, M., Szutowicz, A., Jankowska-Kulawy, A., and  
721 Ronowska, A. (2021). Protection of Cholinergic Neurons against Zinc Toxicity by Glial  
722 Cells in Thiamine-Deficient Media. *Int J Mol Sci* 22. 10.3390/ijms222413337.
- 723 20. Salmina, A.B. (2009). Neuron-glia interactions as therapeutic targets in  
724 neurodegeneration. *J Alzheimers Dis* 16, 485-502. 10.3233/JAD-2009-0988.
- 725 21. Ibrahim, A.M., Pottoo, F.H., Dahiya, E.S., Khan, F.A., and Kumar, J.B.S. (2020).  
726 Neuron-glia interactions: Molecular basis of alzheimer's disease and applications of  
727 neuroproteomics. *Eur J Neurosci* 52, 2931-2943. 10.1111/ejn.14838.
- 728 22. Sheridan, G.K., and Murphy, K.J. (2013). Neuron-glia crosstalk in health and disease:  
729 fractalkine and CX3CR1 take centre stage. *Open Biol* 3, 130181. 10.1098/rsob.130181.
- 730 23. Roh, J.S., and Sohn, D.H. (2018). Damage-Associated Molecular Patterns in  
731 Inflammatory Diseases. *Immune Netw* 18, e27. 10.4110/in.2018.18.e27.
- 732 24. Gong, T., Liu, L., Jiang, W., and Zhou, R. (2020). DAMP-sensing receptors in sterile  
733 inflammation and inflammatory diseases. *Nat Rev Immunol* 20, 95-112.  
734 10.1038/s41577-019-0215-7.
- 735 25. Venegas, C., and Heneka, M.T. (2017). Danger-associated molecular patterns in  
736 Alzheimer's disease. *J Leukoc Biol* 101, 87-98. 10.1189/jlb.3MR0416-204R.
- 737 26. Sasaki, T., Liu, K., Agari, T., Yasuhara, T., Morimoto, J., Okazaki, M., Takeuchi, H.,  
738 Toyoshima, A., Sasada, S., Shinko, A., et al. (2016). Anti-high mobility group box 1  
739 antibody exerts neuroprotection in a rat model of Parkinson's disease. *Exp Neurol* 275  
740 Pt 1, 220-231. 10.1016/j.expneurol.2015.11.003.
- 741 27. Sathe, K., Maetzler, W., Lang, J.D., Mounsey, R.B., Fleckenstein, C., Martin, H.L.,  
742 Schulte, C., Mustafa, S., Synofzik, M., Vukovic, Z., et al. (2012). S100B is increased in  
743 Parkinson's disease and ablation protects against MPTP-induced toxicity through the  
744 RAGE and TNF-alpha pathway. *Brain* 135, 3336-3347. 10.1093/brain/aws250.
- 745 28. Kaur, J., Singh, H., and Naqvi, S. (2023). Intracellular DAMPs in Neurodegeneration  
746 and Their Role in Clinical Therapeutics. *Mol Neurobiol* 60, 3600-3616. 10.1007/s12035-  
747 023-03289-9.
- 748 29. Smeyne, R.J., and Jackson-Lewis, V. (2005). The MPTP model of Parkinson's disease.  
749 *Brain Res Mol Brain Res* 134, 57-66. 10.1016/j.molbrainres.2004.09.017.
- 750 30. Munoz-Manchado, A.B., Villadiego, J., Romo-Madero, S., Suarez-Luna, N., Bermejo-  
751 Navas, A., Rodriguez-Gomez, J.A., Garrido-Gil, P., Labandeira-Garcia, J.L., Echevarria,

- 752 M., Lopez-Barneo, J., and Toledo-Aral, J.J. (2016). Chronic and progressive  
753 Parkinson's disease MPTP model in adult and aged mice. *J Neurochem* 136, 373-387.  
754 10.1111/jnc.13409.
- 755 31. Meller, D., Eysel, U.T., and Schmidt-Kastner, R. (1994). Transient immunohistochemical  
756 labelling of rat retinal axons during Wallerian degeneration by a monoclonal antibody to  
757 neurofilaments. *Brain Res* 648, 162-166. 10.1016/0006-8993(94)91917-8.
- 758 32. Yandamuri, S.S., and Lane, T.E. (2016). Imaging Axonal Degeneration and Repair in  
759 Preclinical Animal Models of Multiple Sclerosis. *Front Immunol* 7, 189.  
760 10.3389/fimmu.2016.00189.
- 761 33. Manivasagam, S., Williams, J.L., Vollmer, L.L., Bollman, B., Bartleson, J.M., Ai, S., Wu,  
762 G.F., and Klein, R.S. (2022). Targeting IFN-lambda Signaling Promotes Recovery from  
763 Central Nervous System Autoimmunity. *J Immunol* 208, 1341-1351.  
764 10.4049/jimmunol.2101041.
- 765 34. Kim, S.T., Son, H.J., Choi, J.H., Ji, I.J., and Hwang, O. (2010). Vertical grid test and  
766 modified horizontal grid test are sensitive methods for evaluating motor dysfunctions in  
767 the MPTP mouse model of Parkinson's disease. *Brain Res* 1306, 176-183.  
768 10.1016/j.brainres.2009.09.103.
- 769 35. Zhang, W., Liu, J., Chen, Q., Ding, W., Li, S., and Ma, L. (2022). Identification of  
770 ADP/ATP Translocase 1 as a Novel Glycoprotein and Its Association with Parkinson's  
771 Disease. *Neurochem Res* 47, 3355-3368. 10.1007/s11064-022-03688-9.
- 772 36. Liddelow, S.A., Guttenplan, K.A., Clarke, L.E., Bennett, F.C., Bohlen, C.J., Schirmer, L.,  
773 Bennett, M.L., Munch, A.E., Chung, W.S., Peterson, T.C., et al. (2017). Neurotoxic  
774 reactive astrocytes are induced by activated microglia. *Nature* 541, 481-487.  
775 10.1038/nature21029.
- 776 37. Yun, S.P., Kam, T.I., Panicker, N., Kim, S., Oh, Y., Park, J.S., Kwon, S.H., Park, Y.J.,  
777 Karuppagounder, S.S., Park, H., et al. (2018). Block of A1 astrocyte conversion by  
778 microglia is neuroprotective in models of Parkinson's disease. *Nat Med* 24, 931-938.  
779 10.1038/s41591-018-0051-5.
- 780 38. Snyder, A.G., Hubbard, N.W., Messmer, M.N., Kofman, S.B., Hagan, C.E., Orozco,  
781 S.L., Chiang, K., Daniels, B.P., Baker, D., and Oberst, A. (2019). Intratumoral activation  
782 of the necroptotic pathway components RIPK1 and RIPK3 potentiates antitumor  
783 immunity. *Sci Immunol* 4. 10.1126/sciimmunol.aaw2004.
- 784 39. Orozco, S.L., Daniels, B.P., Yatim, N., Messmer, M.N., Quarato, G., Chen-Harris, H.,  
785 Cullen, S.P., Snyder, A.G., Ralli-Jain, P., Frase, S., et al. (2019). RIPK3 Activation  
786 Leads to Cytokine Synthesis that Continues after Loss of Cell Membrane Integrity. *Cell*  
787 *Rep* 28, 2275-2287 e2275. 10.1016/j.celrep.2019.07.077.
- 788 40. Orozco, S., Yatim, N., Werner, M.R., Tran, H., Gunja, S.Y., Tait, S.W., Albert, M.L.,  
789 Green, D.R., and Oberst, A. (2014). RIPK1 both positively and negatively regulates  
790 RIPK3 oligomerization and necroptosis. *Cell Death Differ* 21, 1511-1521.  
791 10.1038/cdd.2014.76.
- 792 41. Lier, J., Streit, W.J., and Bechmann, I. (2021). Beyond Activation: Characterizing  
793 Microglial Functional Phenotypes. *Cells* 10. 10.3390/cells10092236.
- 794 42. Kenkhuis, B., Somarakis, A., Kleindouwel, L.R.T., van Roon-Mom, W.M.C., Holtt, T.,  
795 and van der Weerd, L. (2022). Co-expression patterns of microglia markers Iba1,  
796 TMEM119 and P2RY12 in Alzheimer's disease. *Neurobiol Dis* 167, 105684.  
797 10.1016/j.nbd.2022.105684.

- 798 43. Xicoy, H., Wieringa, B., and Martens, G.J. (2017). The SH-SY5Y cell line in Parkinson's  
799 disease research: a systematic review. *Mol Neurodegener* 12, 10. 10.1186/s13024-017-  
800 0149-0.
- 801 44. Nanini, H.F., Bernardazzi, C., Castro, F., and de Souza, H.S.P. (2018). Damage-  
802 associated molecular patterns in inflammatory bowel disease: From biomarkers to  
803 therapeutic targets. *World J Gastroenterol* 24, 4622-4634. 10.3748/wjg.v24.i41.4622.
- 804 45. Andersson, U., Wang, H., Palmblad, K., Aveberger, A.C., Bloom, O., Erlandsson-Harris,  
805 H., Janson, A., Kokkola, R., Zhang, M., Yang, H., and Tracey, K.J. (2000). High mobility  
806 group 1 protein (HMG-1) stimulates proinflammatory cytokine synthesis in human  
807 monocytes. *J Exp Med* 192, 565-570. 10.1084/jem.192.4.565.
- 808 46. Fischer, S., Nasyrov, E., Brosien, M., Preissner, K.T., Marti, H.H., and Kunze, R. (2021).  
809 Self-extracellular RNA promotes pro-inflammatory response of astrocytes to exogenous  
810 and endogenous danger signals. *J Neuroinflammation* 18, 252. 10.1186/s12974-021-  
811 02286-w.
- 812 47. Festoff, B.W., Sajja, R.K., van Dreden, P., and Cucullo, L. (2016). HMGB1 and thrombin  
813 mediate the blood-brain barrier dysfunction acting as biomarkers of neuroinflammation  
814 and progression to neurodegeneration in Alzheimer's disease. *J Neuroinflammation* 13,  
815 194. 10.1186/s12974-016-0670-z.
- 816 48. Banjara, M., and Ghosh, C. (2017). Sterile Neuroinflammation and Strategies for  
817 Therapeutic Intervention. *Int J Inflam* 2017, 8385961. 10.1155/2017/8385961.
- 818 49. Silvis, M.J.M., Kaffka Genaamd Dengler, S.E., Odille, C.A., Mishra, M., van der Kaaij,  
819 N.P., Doevendans, P.A., Sluijter, J.P.G., de Kleijn, D.P.V., de Jager, S.C.A., Bosch, L.,  
820 and van Hout, G.P.J. (2020). Damage-Associated Molecular Patterns in Myocardial  
821 Infarction and Heart Transplantation: The Road to Translational Success. *Front*  
822 *Immunol* 11, 599511. 10.3389/fimmu.2020.599511.
- 823 50. Alisi, A., Carsetti, R., and Nobili, V. (2011). Pathogen- or damage-associated molecular  
824 patterns during nonalcoholic fatty liver disease development. *Hepatology* 54, 1500-  
825 1502. 10.1002/hep.24611.
- 826 51. Brajer-Luftmann, B., Nowicka, A., Kaczmarek, M., Wyrzykiewicz, M., Yasar, S.,  
827 Piorunek, T., Sikora, J., and Batura-Gabryel, H. (2019). Damage-Associated Molecular  
828 Patterns and Myeloid-Derived Suppressor Cells in Bronchoalveolar Lavage Fluid in  
829 Chronic Obstructive Pulmonary Disease Patients. *J Immunol Res* 2019, 9708769.  
830 10.1155/2019/9708769.
- 831 52. Tumburu, L., Ghosh-Choudhary, S., Seifuddin, F.T., Barbu, E.A., Yang, S., Ahmad,  
832 M.M., Wilkins, L.H.W., Tunc, I., Sivakumar, I., Nichols, J.S., et al. (2021). Circulating  
833 mitochondrial DNA is a proinflammatory DAMP in sickle cell disease. *Blood* 137, 3116-  
834 3126. 10.1182/blood.2020009063.
- 835 53. Santilli, F., Vazzana, N., Bucciarelli, L.G., and Davi, G. (2009). Soluble forms of RAGE  
836 in human diseases: clinical and therapeutical implications. *Curr Med Chem* 16, 940-952.  
837 10.2174/092986709787581888.
- 838 54. Sokolove, J., and Lepus, C.M. (2013). Role of inflammation in the pathogenesis of  
839 osteoarthritis: latest findings and interpretations. *Ther Adv Musculoskelet Dis* 5, 77-94.  
840 10.1177/1759720X12467868.
- 841 55. Goldstein, R.S., Gallowitsch-Puerta, M., Yang, L., Rosas-Ballina, M., Huston, J.M.,  
842 Czura, C.J., Lee, D.C., Ward, M.F., Bruchfeld, A.N., Wang, H., et al. (2006). Elevated

- 843 high-mobility group box 1 levels in patients with cerebral and myocardial ischemia.  
844 Shock 25, 571-574. 10.1097/01.shk.0000209540.99176.72.
- 845 56. Teismann, P., Sathe, K., Bierhaus, A., Leng, L., Martin, H.L., Bucala, R., Weigle, B.,  
846 Nawroth, P.P., and Schulz, J.B. (2012). Receptor for advanced glycation endproducts  
847 (RAGE) deficiency protects against MPTP toxicity. Neurobiol Aging 33, 2478-2490.  
848 10.1016/j.neurobiolaging.2011.12.006.
- 849 57. Kong, Z.H., Chen, X., Hua, H.P., Liang, L., and Liu, L.J. (2017). The Oral Pretreatment  
850 of Glycyrrhizin Prevents Surgery-Induced Cognitive Impairment in Aged Mice by  
851 Reducing Neuroinflammation and Alzheimer's-Related Pathology via HMGB1 Inhibition.  
852 J Mol Neurosci 63, 385-395. 10.1007/s12031-017-0989-7.
- 853 58. Langeh, U., and Singh, S. (2021). Targeting S100B Protein as a Surrogate Biomarker  
854 and its Role in Various Neurological Disorders. Curr Neuropharmacol 19, 265-277.  
855 10.2174/1570159X18666200729100427.
- 856 59. Brambilla, L., Martorana, F., Guidotti, G., and Rossi, D. (2018). Dysregulation of  
857 Astrocytic HMGB1 Signaling in Amyotrophic Lateral Sclerosis. Front Neurosci 12, 622.  
858 10.3389/fnins.2018.00622.
- 859 60. Cristovao, J.S., Morris, V.K., Cardoso, I., Leal, S.S., Martinez, J., Botelho, H.M., Gobl,  
860 C., David, R., Kierdorf, K., Alemi, M., et al. (2018). The neuronal S100B protein is a  
861 calcium-tuned suppressor of amyloid-beta aggregation. Sci Adv 4, eaaq1702.  
862 10.1126/sciadv.aaq1702.
- 863 61. Huttunen, H.J., Kuja-Panula, J., Sorci, G., Agneletti, A.L., Donato, R., and Rauvala, H.  
864 (2000). Coregulation of neurite outgrowth and cell survival by amphoterin and S100  
865 proteins through receptor for advanced glycation end products (RAGE) activation. J Biol  
866 Chem 275, 40096-40105. 10.1074/jbc.M006993200.
- 867 62. Druse, M.J., Gillespie, R.A., Tajuddin, N.F., and Rich, M. (2007). S100B-mediated  
868 protection against the pro-apoptotic effects of ethanol on fetal rhombencephalic  
869 neurons. Brain Res 1150, 46-54. 10.1016/j.brainres.2007.02.092.
- 870 63. Businaro, R., Leone, S., Fabrizi, C., Sorci, G., Donato, R., Lauro, G.M., and Fumagalli,  
871 L. (2006). S100B protects LAN-5 neuroblastoma cells against Abeta amyloid-induced  
872 neurotoxicity via RAGE engagement at low doses but increases Abeta amyloid  
873 neurotoxicity at high doses. J Neurosci Res 83, 897-906. 10.1002/jnr.20785.
- 874 64. Sorci, G., Bianchi, R., Riuzzi, F., Tubaro, C., Arcuri, C., Giambanco, I., and Donato, R.  
875 (2010). S100B Protein, A Damage-Associated Molecular Pattern Protein in the Brain  
876 and Heart, and Beyond. Cardiovasc Psychiatry Neurol 2010. 10.1155/2010/656481.
- 877 65. Juranek, J., Mukherjee, K., Kordas, B., Zalecki, M., Korytko, A., Zglejc-Waszak, K.,  
878 Szuszkiewicz, J., and Banach, M. (2022). Role of RAGE in the Pathogenesis of  
879 Neurological Disorders. Neurosci Bull 38, 1248-1262. 10.1007/s12264-022-00878-x.
- 880 66. Song, J., Lee, W.T., Park, K.A., and Lee, J.E. (2014). Receptor for advanced glycation  
881 end products (RAGE) and its ligands: focus on spinal cord injury. Int J Mol Sci 15,  
882 13172-13191. 10.3390/ijms150813172.
- 883 67. Kim, J., Waldvogel, H.J., Faull, R.L., Curtis, M.A., and Nicholson, L.F. (2015). The  
884 RAGE receptor and its ligands are highly expressed in astrocytes in a grade-dependant  
885 manner in the striatum and subependymal layer in Huntington's disease. J Neurochem  
886 134, 927-942. 10.1111/jnc.13178.
- 887 68. Serrano, A., Donno, C., Giannetti, S., Peric, M., Andjus, P., D'Ambrosi, N., and Michetti,  
888 F. (2017). The Astrocytic S100B Protein with Its Receptor RAGE Is Aberrantly

- 889 Expressed in SOD1(G93A) Models, and Its Inhibition Decreases the Expression of  
890 Proinflammatory Genes. *Mediators Inflamm* 2017, 1626204. 10.1155/2017/1626204.
- 891 69. Shi, J., Xu, H., Cavagnaro, M.J., Li, X., and Fang, J. (2021). Blocking HMGB1/RAGE  
892 Signaling by Berberine Alleviates A1 Astrocyte and Attenuates Sepsis-Associated  
893 Encephalopathy. *Front Pharmacol* 12, 760186. 10.3389/fphar.2021.760186.
- 894 70. Ponath, G., Schettler, C., Kaestner, F., Voigt, B., Wentker, D., Arolt, V., and  
895 Rothermundt, M. (2007). Autocrine S100B effects on astrocytes are mediated via  
896 RAGE. *J Neuroimmunol* 184, 214-222. 10.1016/j.jneuroim.2006.12.011.
- 897 71. Villarreal, A., Seoane, R., Gonzalez Torres, A., Rosciszewski, G., Angelo, M.F., Rossi,  
898 A., Barker, P.A., and Ramos, A.J. (2014). S100B protein activates a RAGE-dependent  
899 autocrine loop in astrocytes: implications for its role in the propagation of reactive  
900 gliosis. *J Neurochem* 131, 190-205. 10.1111/jnc.12790.
- 901 72. Ding, S., Wang, C., Wang, W., Yu, H., Chen, B., Liu, L., Zhang, M., and Lang, Y.  
902 (2021). Autocrine S100B in astrocytes promotes VEGF-dependent inflammation and  
903 oxidative stress and causes impaired neuroprotection. *Cell Biol Toxicol*.  
904 10.1007/s10565-021-09674-1.
- 905 73. Przedborski, S., Jackson-Lewis, V., Naini, A.B., Jakowec, M., Petzinger, G., Miller, R.,  
906 and Akram, M. (2001). The parkinsonian toxin 1-methyl-4-phenyl-1,2,3,6-  
907 tetrahydropyridine (MPTP): a technical review of its utility and safety. *J Neurochem* 76,  
908 1265-1274. 10.1046/j.1471-4159.2001.00183.x.
- 909 74. Lin, Q.S., Chen, P., Wang, W.X., Lin, C.C., Zhou, Y., Yu, L.H., Lin, Y.X., Xu, Y.F., and  
910 Kang, D.Z. (2020). RIP1/RIP3/MLKL mediates dopaminergic neuron necroptosis in a  
911 mouse model of Parkinson disease. *Lab Invest* 100, 503-511. 10.1038/s41374-019-  
912 0319-5.
- 913 75. Dionisio, P.A., Oliveira, S.R., Gaspar, M.M., Gama, M.J., Castro-Caldas, M., Amaral,  
914 J.D., and Rodrigues, C.M.P. (2019). Ablation of RIP3 protects from dopaminergic  
915 neurodegeneration in experimental Parkinson's disease. *Cell Death Dis* 10, 840.  
916 10.1038/s41419-019-2078-z.
- 917 76. Wehn, A.C., Khalin, I., Duering, M., Hellal, F., Culmsee, C., Vandenabeele, P., Plesnila,  
918 N., and Terpolilli, N.A. (2021). RIPK1 or RIPK3 deletion prevents progressive neuronal  
919 cell death and improves memory function after traumatic brain injury. *Acta Neuropathol*  
920 *Commun* 9, 138. 10.1186/s40478-021-01236-0.
- 921 77. Ito, Y., Ofengeim, D., Najafov, A., Das, S., Saberi, S., Li, Y., Hitomi, J., Zhu, H., Chen,  
922 H., Mayo, L., et al. (2016). RIPK1 mediates axonal degeneration by promoting  
923 inflammation and necroptosis in ALS. *Science* 353, 603-608. 10.1126/science.aaf6803.
- 924 78. Faust, H., Lam, L.M., Hotz, M.J., Qing, D., and Mangalmurti, N.S. (2020). RAGE  
925 interacts with the necroptotic protein RIPK3 and mediates transfusion-induced danger  
926 signal release. *Vox Sang* 115, 729-734. 10.1111/vox.12946.
- 927 79. Boytard, L., Hadi, T., Silvestro, M., Qu, H., Kumpfbeck, A., Sleiman, R., Fils, K.H.,  
928 Alebrahim, D., Boccalatte, F., Kugler, M., et al. (2020). Lung-derived HMGB1 is  
929 detrimental for vascular remodeling of metabolically imbalanced arterial macrophages.  
930 *Nat Commun* 11, 4311. 10.1038/s41467-020-18088-2.
- 931 80. Wen, S., Li, X., Ling, Y., Chen, S., Deng, Q., Yang, L., Li, Y., Shen, J., Qiu, Y., Zhan, Y.,  
932 et al. (2020). HMGB1-associated necroptosis and Kupffer cells M1 polarization  
933 underlies remote liver injury induced by intestinal ischemia/reperfusion in rats. *FASEB J*  
934 34, 4384-4402. 10.1096/fj.201900817R.

- 935 81. Minsart, C., Liefferinckx, C., Lemmers, A., Dressen, C., Quertinmont, E., Leclercq, I.,  
936 Deviere, J., Moreau, R., and Gustot, T. (2020). New insights in acetaminophen toxicity:  
937 HMGB1 contributes by itself to amplify hepatocyte necrosis in vitro through the TLR4-  
938 TRIF-RIPK3 axis. *Sci Rep* 10, 5557. 10.1038/s41598-020-61270-1.
- 939 82. Meng, R., Gu, L., Lu, Y., Zhao, K., Wu, J., Wang, H., Han, J., Tang, Y., and Lu, B.  
940 (2019). High mobility group box 1 enables bacterial lipids to trigger receptor-interacting  
941 protein kinase 3 (RIPK3)-mediated necroptosis and apoptosis in mice. *J Biol Chem* 294,  
942 8872-8884. 10.1074/jbc.RA118.007040.
- 943 83. Sparvero, L.J., Asafu-Adjei, D., Kang, R., Tang, D., Amin, N., Im, J., Rutledge, R., Lin,  
944 B., Amoscato, A.A., Zeh, H.J., and Lotze, M.T. (2009). RAGE (Receptor for Advanced  
945 Glycation Endproducts), RAGE ligands, and their role in cancer and inflammation. *J*  
946 *Transl Med* 7, 17. 10.1186/1479-5876-7-17.
- 947 84. Kierdorf, K., and Fritz, G. (2013). RAGE regulation and signaling in inflammation and  
948 beyond. *J Leukoc Biol* 94, 55-68. 10.1189/jlb.1012519.
- 949 85. Bianchi, R., Adami, C., Giambanco, I., and Donato, R. (2007). S100B binding to RAGE  
950 in microglia stimulates COX-2 expression. *J Leukoc Biol* 81, 108-118.  
951 10.1189/jlb.0306198.
- 952 86. Lander, H.M., Tauras, J.M., Ogiste, J.S., Hori, O., Moss, R.A., and Schmidt, A.M.  
953 (1997). Activation of the receptor for advanced glycation end products triggers a  
954 p21(ras)-dependent mitogen-activated protein kinase pathway regulated by oxidant  
955 stress. *J Biol Chem* 272, 17810-17814. 10.1074/jbc.272.28.17810.
- 956 87. Lee, K.J., Yoo, J.W., Kim, Y.K., Choi, J.H., Ha, T.Y., and Gil, M. (2018). Advanced  
957 glycation end products promote triple negative breast cancer cells via ERK and NF-  
958 kappaB pathway. *Biochem Biophys Res Commun* 495, 2195-2201.  
959 10.1016/j.bbrc.2017.11.182.
- 960 88. Marsche, G., Semlitsch, M., Hammer, A., Frank, S., Weigle, B., Demling, N., Schmidt,  
961 K., Windischhofer, W., Waeg, G., Sattler, W., and Malle, E. (2007). Hypochlorite-  
962 modified albumin colocalizes with RAGE in the artery wall and promotes MCP-1  
963 expression via the RAGE-Erk1/2 MAP-kinase pathway. *FASEB J* 21, 1145-1152.  
964 10.1096/fj.06-7439com.
- 965 89. Yatim, N., Jusforgues-Saklani, H., Orozco, S., Schulz, O., Barreira da Silva, R., Reis e  
966 Sousa, C., Green, D.R., Oberst, A., and Albert, M.L. (2015). RIPK1 and NF-kappaB  
967 signaling in dying cells determines cross-priming of CD8(+) T cells. *Science* 350, 328-  
968 334. 10.1126/science.aad0395.
- 969 90. Liu, J., Zhu, Z., Wang, L., Du, J., Zhang, B., Feng, X., and Zhang, G. (2020). Functional  
970 suppression of Ripk1 blocks the NF-kappaB signaling pathway and induces neuron  
971 autophagy after traumatic brain injury. *Mol Cell Biochem* 472, 105-114.  
972 10.1007/s11010-020-03789-5.
- 973 91. Yu, P.W., Huang, B.C., Shen, M., Quast, J., Chan, E., Xu, X., Nolan, G.P., Payan, D.G.,  
974 and Luo, Y. (1999). Identification of RIP3, a RIP-like kinase that activates apoptosis and  
975 NFkappaB. *Curr Biol* 9, 539-542. 10.1016/s0960-9822(99)80239-5.
- 976 92. Newton, K., Sun, X., and Dixit, V.M. (2004). Kinase RIP3 is dispensable for normal NF-  
977 kappa Bs, signaling by the B-cell and T-cell receptors, tumor necrosis factor receptor 1,  
978 and Toll-like receptors 2 and 4. *Mol Cell Biol* 24, 1464-1469. 10.1128/MCB.24.4.1464-  
979 1469.2004.



- 980 93. Murphy, J.M., Czabotar, P.E., Hildebrand, J.M., Lucet, I.S., Zhang, J.G., Alvarez-Diaz,  
981 S., Lewis, R., Lalaoui, N., Metcalf, D., Webb, A.I., et al. (2013). The pseudokinase  
982 MLKL mediates necroptosis via a molecular switch mechanism. *Immunity* 39, 443-453.  
983 10.1016/j.immuni.2013.06.018.
- 984 94. Jackson-Lewis, V., and Przedborski, S. (2007). Protocol for the MPTP mouse model of  
985 Parkinson's disease. *Nat Protoc* 2, 141-151. 10.1038/nprot.2006.342.
- 986 95. Daniels, B.P., Jujjavarapu, H., Durrant, D.M., Williams, J.L., Green, R.R., White, J.P.,  
987 Lazear, H.M., Gale, M., Jr., Diamond, M.S., and Klein, R.S. (2017). Regional astrocyte  
988 IFN signaling restricts pathogenesis during neurotropic viral infection. *J Clin Invest* 127,  
989 843-856. 10.1172/JCI88720.

990